

Numerical Modelling of Buoyancy Induced Flow in Earth's Mantle: Application to Global Geophysical Surface Observables

Alessandro Forte

フォルテ

アレックス

強

荒楠

Proposed (Tentative!) Outline of Lecture

1. Introduction

- thermal convection modelling and global seismic tomography
- present-day mantle dynamics and convection-related surface observables

2. Spectral Modelling of Viscous Mantle Flow in 3-D Spherical Geometry

- general hydrodynamic equations and simplifications for the mantle

Analytical Models of Incompressible Flow:

- poloidal and toroidal flow equations
- poloidal Green functions
- geodynamic kernel functions for surface observables

Numerical Models of Compressible Flow:

- covariant tensor equations: generalized spherical harmonics
- poloidal and toroidal systems of flow equations
- internal boundary conditions: phase-change and chemical boundaries
- surface boundary conditions
- treatment of hydrostatic perturbations in the core
- re-normalized flow equations using logarithmic viscosity and density

3. **Modelling Convection-Related Surface Observables**

- recent radial viscosity inferences
- geodynamic kernel functions
- predicted surface observables based on seismic tomography

4. **Concluding Comments**

- preview of next lecture:

Modelling Mantle Dynamics with Rigid Tectonic Plates and Internal Viscosity Heterogeneity

1. Introduction

We will focus on the *dynamics of the mantle* and, in particular on how the internal dynamics are manifested at the Earth's surface. It is now generally accepted that an understanding of thermal convection in the mantle is necessary for explaining a multitude of geophysical and geological processes which we can observe and measure at the surface of the Earth, such as continental drift, earthquakes, mountain building, volcanism, perturbations in Earth's gravitational field, variations in oceanic bathymetry and continental elevation, and long-term changes in global sea-level variations, to name just a few.

The mathematical and numerical models which will be presented here are undoubtedly greatly simplified representations of the actual physical processes occurring deep inside our planet. We must therefore recognize the need for caution when using these models to investigate convection dynamics in the mantle. I expect, nonetheless, that the models we will develop here will allow us to grasp some of the essential aspects of the physics needed to understand mantle dynamics.

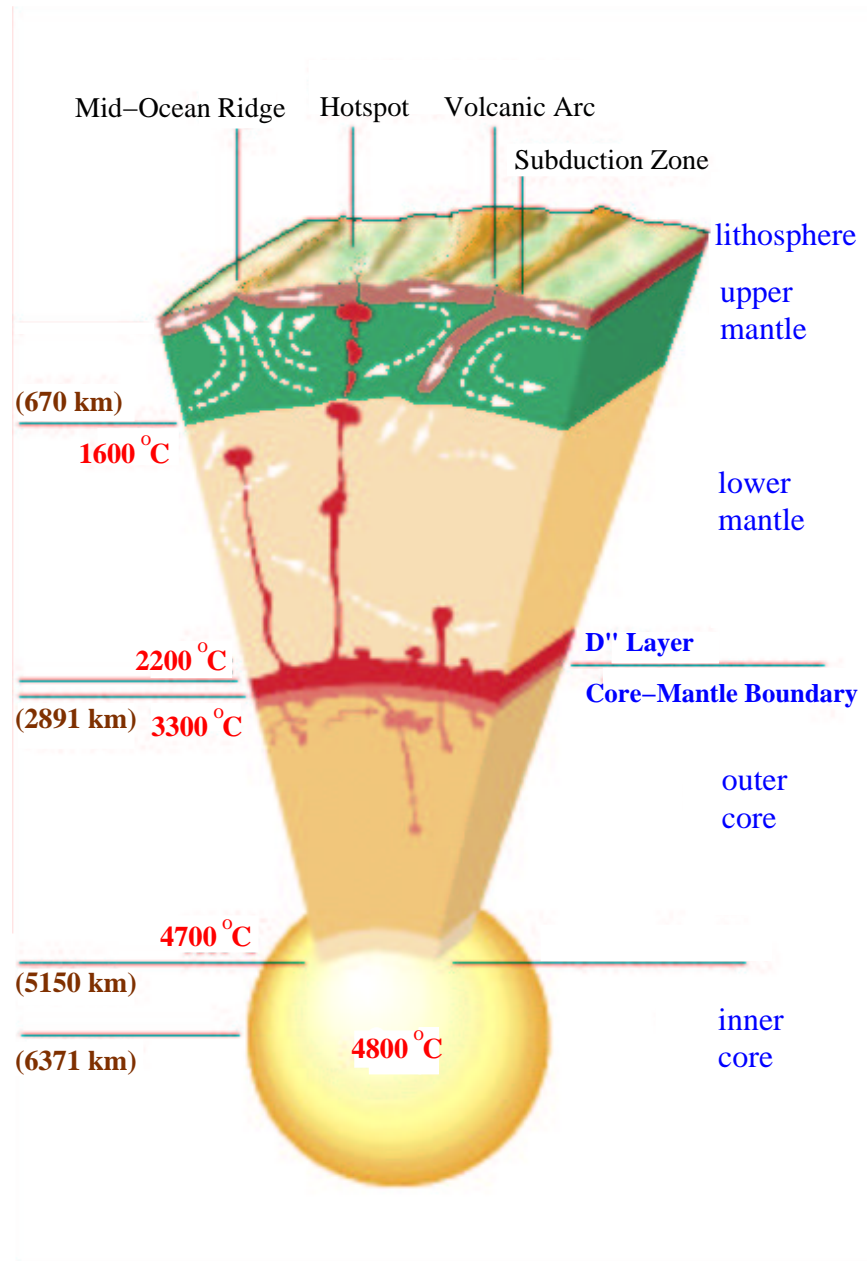


Fig. 1. An 'artistic' view of Earth's internal dynamics [adapted from *Besse & Courtillot*]

1.1. Understanding convection dynamics in the mantle

Schematic or artistic illustrations of Earth's internal dynamics, such as in Fig. 1, are useful for helping to establish the main questions we wish to resolve in order to elucidate our understanding of mantle convection and its impact of surface processes. For example, do subducted slabs descend continuously across the mantle or are they deflected at the seismic horizon separating the upper and lower mantle? Do thermal plumes erupt from the base of the mantle and do they ascend right up to the surface to give rise to hotspots and perhaps also drive sea-floor spreading along mid-ocean ridges? These are some of the basic questions which geophysicists are still seeking to clarify.

We must therefore develop models of thermal convection dynamics which we hope are sufficiently realistic. There are now three basic approaches we can take in developing these models: (1) numerical computer-based simulations, (2) flow modelling based on seismic tomographic images of mantle structure, and (3) controlled fluid mechanical experiments in a laboratory.

The first approach is, by far, the most popular and it has a long history, dating back to the classical work of *McKenzie et al.* [1974]. This paper established a path

which has been followed by a large number of subsequent numerical studies which are far too numerous to cite here.

The basic governing principles needed for the numerical simulation of thermal convection are:

- conservation of mass
- conservation of momentum
- conservation of energy
- ‘conservation’ of gravity (Poisson’s equation)

The resolution of these conservation laws requires the following supplementary equations which are specific to the mantle:

- dependence of stress on strain rate (constitutive relation)
- an equation of state which expresses the dependence of density on temperature and pressure (and perhaps on chemical composition)

The following is a *non-dimensional* mathematical representation of the governing

equations:

- conservation of mass

$$\frac{\partial \rho}{\partial t} + \vec{\nabla} \cdot (\rho \vec{u}) = 0 \Rightarrow \vec{\nabla} \cdot (\rho_r \vec{u}) = 0$$

- conservation of momentum

$$\begin{aligned} \rho \frac{Ra}{Pr} \frac{d\vec{u}}{dt} &= \frac{1}{\alpha \Delta T} \left(-\vec{\nabla} P + \rho \vec{g} \right) + \vec{\nabla} \cdot \vec{\bar{\tau}} \\ \Rightarrow \frac{1}{\alpha \Delta T} \left(-\vec{\nabla} P + \rho \vec{g} \right) + \vec{\nabla} \cdot \vec{\bar{\tau}} &= 0 \end{aligned}$$

- conservation of energy

$$\begin{aligned} \frac{\partial T}{\partial t} &= - \underbrace{\vec{u} \cdot \vec{\nabla} T}_{\text{advection}} + \underbrace{\frac{1}{\rho_r Ra} \vec{\nabla} \cdot k \vec{\nabla} T}_{\text{diffusion}} + \underbrace{\frac{Q}{\rho_r Ra}}_{\text{internal heat}} \\ &+ \frac{\lambda}{\rho} \underbrace{\left(T \frac{Dp}{Dt} + \Phi \right)}_{\text{compressible effects}} \end{aligned}$$

These governing equations are characterized by the following parameters:

Scaling parameters:

Temperature: $\Delta T = 3700$ K

Length: $d = 2888$ km

Velocity: $U = \frac{\rho_0 g_0 \alpha \Delta T d^2}{\eta}$

Non-dimensional parameters:

Rayleigh number: $Ra = \frac{\rho^2 c_p g \alpha \Delta T d^3}{k \eta}$

Prandtl number: $Pr = \frac{\nu}{\kappa}$

Dissipation number: $\lambda = \frac{g_0 \alpha d}{c_p}$

The equation which arguably presents the greatest challenge (and the most mathematical and computational difficulty) is the *conservation of energy equation*.

Some of the major complexities presented by this equation are:

- Very high Rayleigh number ($\sim 10^7, 10^8$) \Rightarrow narrow thermal boundary layers and highly time-dependent convection
- depth-dependence of density and gravity are non-negligible \Rightarrow viscous dissipation (i.e., Dissipation number) is important
- highly nonlinear feedback from strongly temperature-dependent viscosity
- phase transitions (400 and 670 km depth)
- poorly constrained knowledge of internal (radiogenic) heating distribution

In spite of the significant computational difficulties in obtaining 'realistic' numerical simulations of mantle convection, there has been encouraging progress over the past few years, as is illustrated in the following figure:

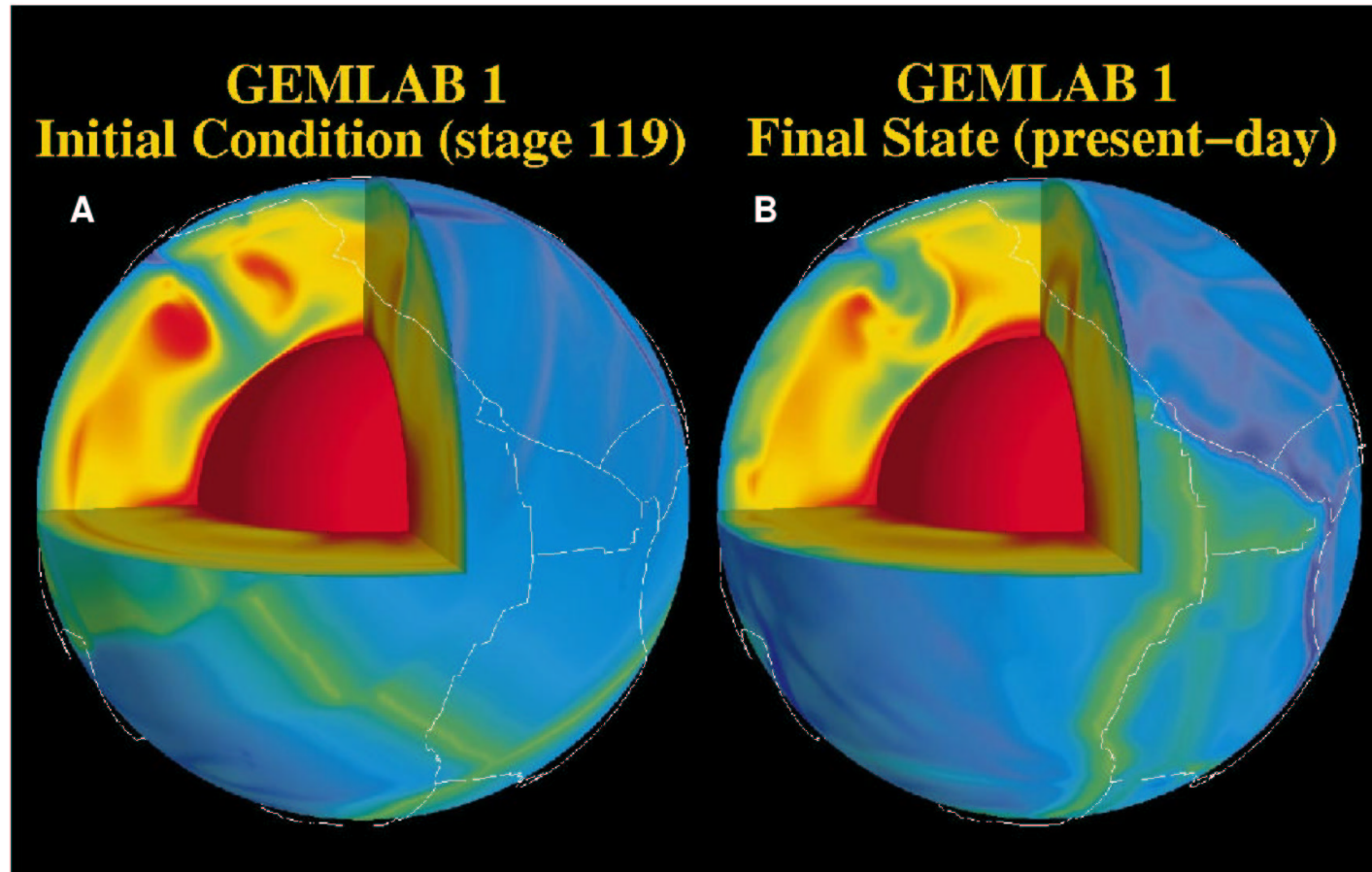


Fig. 2. Numerical convection simulation incorporating time-dependent plate-tectonics (from *Bunge et al.* [1998])

1.2. Mantle convection and global seismic tomography

The time-dependent convection simulation in Fig. 2, shows a dynamical regime which is almost completely dominated by cold descending plumes which correspond to subducted slab heterogeneity. This dominance arises from the assumption of strong internal heating, which is compensated by cooling from above, and it is characterized by the absence of active hot plumes ascending from the CMB.

The convection simulation in Fig. 2 predicts a pattern of thermal heterogeneity which appears to be quite different from that revealed by global *seismic tomographic imaging*. Global tomography models have consistently revealed the presence of major plume-like structures in the deep mantle. The presence of such deep-seated plumes is clearly apparent in Fig. 3 which shows the S-wave heterogeneity in the tomography model *SH12_WM13* of *Su et al.* [1994].

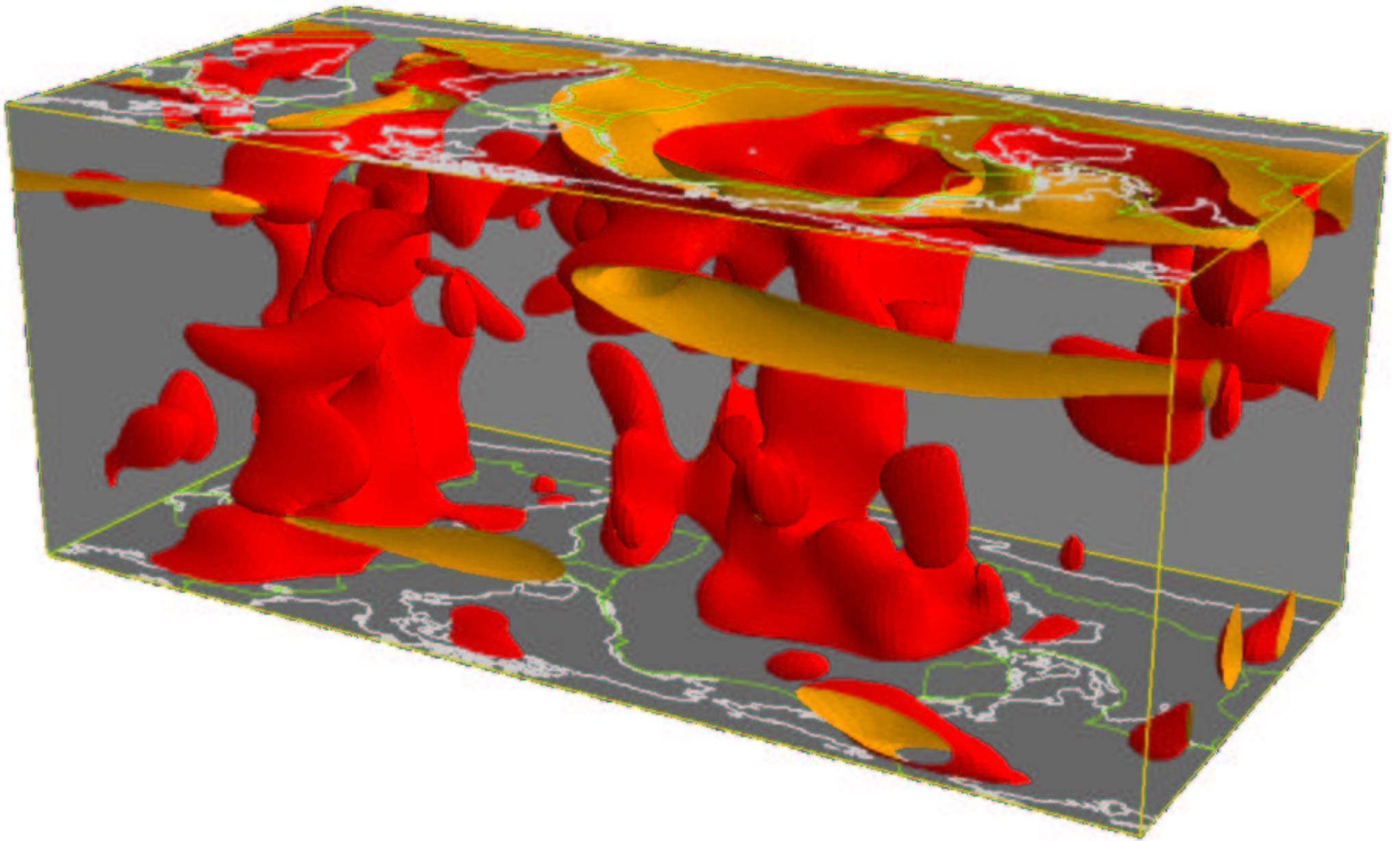


Fig. 3. Mantle heterogeneity (from *Su et al.* [1994]) for all regions in which $\delta V_s/V_s < -0.6\%$.

The significant discrepancies between the recent numerical convection simulations (e.g., Fig. 2) and the seismic tomographic images (e.g., Fig. 3) are a reminder of the progress which must still be made before the purely numerical convection simulation can properly explain the structure and evolution of 3-D mantle structure. These difficulties suggest a *second approach for modelling mantle dynamics*, namely to use the mantle structure revealed by the tomography models as a proxy for the thermal anomalies which are maintained by the thermal convection process in the mantle.

This tomography-based modelling of the mantle convective flow is equivalent to assuming that the conservation of energy equation has already been ‘solved’ (at least for the present-day temperature anomalies) by global seismic tomographic imaging.

In the following we will carry out a detailed development of this alternative approach to the study of convection dynamics in the mantle. We will therefore focus on models which can predict the 3-D buoyancy-induced flow corresponding to seismically imaged mantle heterogeneity. We will apply these flow models to explore the relationship between seismically inferred 3-D mantle

structure and the various surface manifestations of convection dynamics.

With this alternative approach to modelling mantle dynamics we can fully exploit the detailed heterogeneity revealed by the most recent global tomography models, as in the following figure.

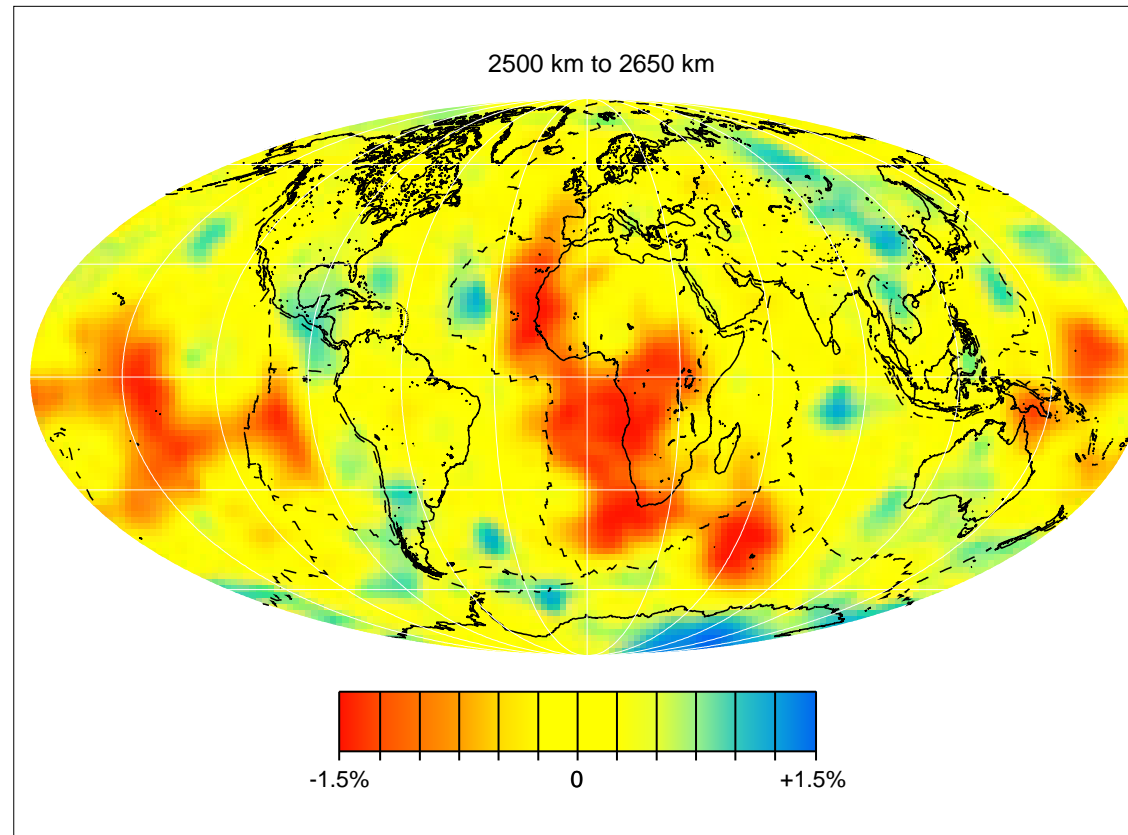


Fig. 4. Lower-mantle S-wave heterogeneity [Grand, 2002].

2. Spectral Mantle Flow Models in 3-D Spherical Geometry

2.1. General hydrodynamic equations

The hydrodynamic field equations (*Landau and Lifshitz, 1959*) which express the principles of conservation of mass and momentum are

$$\frac{\partial \rho}{\partial t} + \nabla \cdot (\rho \mathbf{u}) = 0 \quad (1)$$

$$\rho \frac{d\mathbf{u}}{dt} = \nabla \cdot \boldsymbol{\sigma} + \rho \mathbf{g} \quad (2)$$

in which \mathbf{u} is the velocity field, $\boldsymbol{\sigma}$ the stress tensor, \mathbf{g} the gravitational acceleration and ρ the density.

We may represent the gravity field \mathbf{g} in terms of a gravitational potential:

$$\mathbf{g} = \nabla \phi \quad (3)$$

Notice that the sign convention adopted here is opposite to that generally adopted in classical physics, where a *negative* gradient of the potential is used.

With this sign convention, Poisson's equation for the relationship between the gravity potential and density is:

$$\Delta\phi = -4\pi G\rho \quad (\Delta \equiv \nabla \cdot \nabla) \quad (4)$$

An explicit expression for the stress tensor is given by

$$\sigma_{ij} = -P\delta_{ij} + \tau_{ij} \quad (5)$$

$$\text{with } \tau_{ij} = \eta \left(u_{i,j} + u_{j,i} - \frac{2}{3}\delta_{ij}u_{k,k} \right) + \lambda\delta_{ij}u_{k,k} \quad (6)$$

where τ_{ij} is the viscous stress tensor, δ_{ij} is the identity tensor, P is the total pressure, η and λ are the *isotropic* viscosity coefficients, and $u_{i,j} = \partial u_i / \partial x_j$ represents the derivative of the velocity components i with respect to the coordinate direction j .

2.2. Simplifications appropriate for the mantle

- The “second” viscosity coefficient λ in the viscous stress tensor τ_{ij} describes the dissipation associated with change in fluid volume (density).

This volume dissipation may be neglected if the changes in fluid volume occur on time scales which are much longer than for molecular relaxation processes (*Landau and Lifshitz, 1959*), and this is certainly true for mantle flow. Therefore, the viscous stress tensor τ_{ij} will be purely deviatoric:

$$\tau_{ij} = \eta \left(u_{i,j} + u_{j,i} - \frac{2}{3} \delta_{ij} u_{k,k} \right) \quad (7)$$

- We will further assume a *Newtonian* (i.e. linear) rheology, in which the mantle viscosity η is not a function of stress or strain-rate. This assumption is not necessarily ‘appropriate’ for the mantle (particularly in high stress regions, such as subduction zones) but it will greatly simplify the mathematical resolution of the flow equations which is presented below.
- Since mantle rocks creep much slower than the acoustic velocity in the mantle, we can safely ignore the term $\partial\rho/\partial t$ in the conservation of mass equation (1) and we thus have the following *anelastic-liquid* approximation:

$$\nabla \cdot (\rho \mathbf{u}) = 0 \quad (8)$$

- We may non-dimensionalize the conservation of momentum equation with the following variable transformations:

$$(x, y, z) = (d x, d y, d z)$$

$$t = (d^2 / \kappa_o) t$$

$$\rho = \rho_o \rho; \mathbf{g} = \mathbf{g}_o \mathbf{g}; \eta = \eta_o \eta$$

where the original variables are on the left and the non-dimensional ones are on the right. The length scale d is arbitrary and $\kappa_o, \rho_o, \eta_o, \mathbf{g}_o$ are characteristic thermal diffusivity, density, viscosity, and gravitational acceleration, respectively, in the mantle.

Employing these variable transformations [and after substituting (5) & (7) into (2)], the non-dimensional momentum conservation equation is:

$$\left(\frac{\nu_o}{d^2}\right) \left(\frac{\kappa_o}{d^2}\right) \left(\frac{d}{\mathbf{g}_o}\right) \left[\frac{1}{Pr} \rho \frac{d\mathbf{u}}{dt} - \nabla \cdot \boldsymbol{\tau} \right] = -\nabla P + \rho \mathbf{g}$$

in which $\nu_o = \eta_o / \rho_o$ is the *kinematic viscosity* and the non-dimensional number $Pr = \nu_o / \kappa_o$ is called the *Prandtl number*.

The Prandtl number is a ratio of thermal diffusion over momentum diffusion time scales and for the mantle it is estimated to be extremely large and is effectively treated as infinite:

$$Pr \simeq 10^{24}$$

For an infinite Prandtl number the inertial force term $\rho d\mathbf{u}/dt$ in the momentum conservation equation (2) may be set to zero and, also using expression (3), we then obtain:

$$\nabla \cdot \boldsymbol{\tau} - \nabla P + \rho \nabla \phi = \mathbf{0} \quad (9)$$

Equation (9) shows that in the absence of inertia, there must at all times be a balance between the buoyancy forces ρg and the forces of viscous dissipation described by $\nabla \cdot \boldsymbol{\tau}$. In other words, any changes in internal buoyancy forces will *instantly* produce changes in fluid flow: this is a consequence of the infinite-Prandtl number approximation.

2.3. Hydrostatic reference state

We may define an idealized *hydrostatic reference state* for the mantle, which

corresponds to the absence of any internal flow or deformation (i.e. $\mathbf{u} = \mathbf{0}$). In this situation the deviatoric stress field $\boldsymbol{\tau}$ vanishes and the momentum conservation equation (2) reduces to:

$$-\nabla P_o + \rho_o \nabla \phi_o = \mathbf{0} \quad (10)$$

in which P_o , ρ_o , and ϕ_o are the pressure, density and gravity potentials in the hydrostatic state. Poisson's equation (4) for a hydrostatic planet is:

$$\Delta \phi_o = -4\pi G \rho_o \quad (11)$$

2.4. Non-hydrostatic dynamical equations

We assume that in a dynamic mantle, with a non-vanishing mantle flow \mathbf{u} , the pressure, density and gravity potentials will be perturbed as follows:

$$P = P_o + P_1 \quad \rho = \rho_o + \rho_1 \quad \phi = \phi_o + \phi_1 \quad (12)$$

in which all perturbations are assumed to be *small*, that is:

$$\left| \frac{P_1}{P_o} \right| \ll 1 \quad \left| \frac{\rho_1}{\rho_o} \right| \ll 1 \quad \left| \frac{\phi_1}{\phi_o} \right| \ll 1$$

If we now substitute the perturbed variables (12) into the equations of mass and momentum conservation (8–9) and Poisson’s equation (4), and then subtract out the hydrostatic reference equations (10–11), we finally obtain the following set of *first-order accurate, perturbed equations* for mantle flow dynamics:

<i>mass conservation</i>	$\nabla \cdot (\rho_o \mathbf{u}) = 0$	(13)
<i>momentum conservation</i>	$\nabla \cdot \boldsymbol{\tau} - \nabla P_1 + \underbrace{\rho_o \nabla \phi_1}_{\text{self-gravity}} + \underbrace{\rho_1 \nabla \phi_o}_{\text{buoyancy force}} = \mathbf{0}$	(14)
<i>gravity ‘conservation’</i>	$\Delta \phi_1 = -4\pi G \rho_1$	(15)

Notice in equation (14), that in addition to the driving *buoyancy forces*, there also exist *self-gravitational loads* due to the perturbed gravity field. The above equations must be supplemented by the linear relationship (7) between stress and strain-rate, which is valid for an *isotropic* rheology:

<i>Newtonian constitutive equation</i>	$\boldsymbol{\tau} = \eta \left(\overrightarrow{\nabla} \mathbf{u} + \mathbf{u} \overleftarrow{\nabla} - \frac{2}{3} \mathbf{I} \nabla \cdot \mathbf{u} \right)$	(16)
--	---	------

2.5. Analytical solutions for incompressible mantle flow

2.5.1 poloidal and toroidal classes of flow

If we assume the mantle flow is *incompressible*, this implies that any parcel of mantle material will not experience any change in density along its trajectory:

$$\frac{d\rho}{dt} = \frac{\partial\rho}{\partial t} + \mathbf{u} \cdot \nabla\rho = 0$$

On the basis of this expression, we immediately see that the original mass-conservation equation (1) becomes:

$$\nabla \cdot \mathbf{u} = 0 \tag{17}$$

Equation (17) shows that an incompressible flow \mathbf{u} is a *solenoidal* vector field (like the magnetic field \mathbf{B}). *Backus* [1958] proved that any solenoidal vector field may be expressed in terms of two scalar potential functions as follows:

$$\mathbf{u} = \nabla \times \Lambda p + \Lambda q \tag{18}$$

$$\text{where } \Lambda = \mathbf{r} \times \nabla \tag{19}$$

in which p and q are the *poloidal* and *toroidal* flow scalars, respectively.

On the basis of expression (18) we can show that the *horizontal divergence* of the flow, expressed in spherical coordinates, is

$$\nabla_{\mathbf{H}} \cdot \mathbf{u} = -\frac{\Lambda^2}{r^2} \frac{\partial}{\partial r} r p \quad (20)$$

where $\Lambda^2 = \mathbf{\Lambda} \cdot \mathbf{\Lambda}$ is the horizontal part of the Laplacian operator $\Delta (= \nabla^2)$:

$$\Delta = \frac{1}{r} \frac{\partial^2}{\partial r^2} r + \frac{1}{r^2} \Lambda^2 \quad (21)$$

From equation (18) we can similarly show that the *radial vorticity* of the flow, expressed in spherical coordinates, is

$$\hat{\mathbf{r}} \cdot \nabla \times \mathbf{u} = \frac{1}{r} \mathbf{\Lambda} \cdot \mathbf{u} = \frac{\Lambda^2}{r} q \quad (22)$$

in which $\hat{\mathbf{r}}$ is the unit radius vector.

From (20, 22) we can immediately conclude that the *horizontal divergence* of the surface tectonic plate motions, which describes plate motions at *mid-ocean ridges* and at *subduction zones*, corresponds to poloidal flow [Forte & Peltier, 1987]. Similarly, as Forte & Peltier [1987] showed, the *radial vorticity* of the plate motions, which describes plate motions along *transform boundaries*, corresponds to toroidal flow.

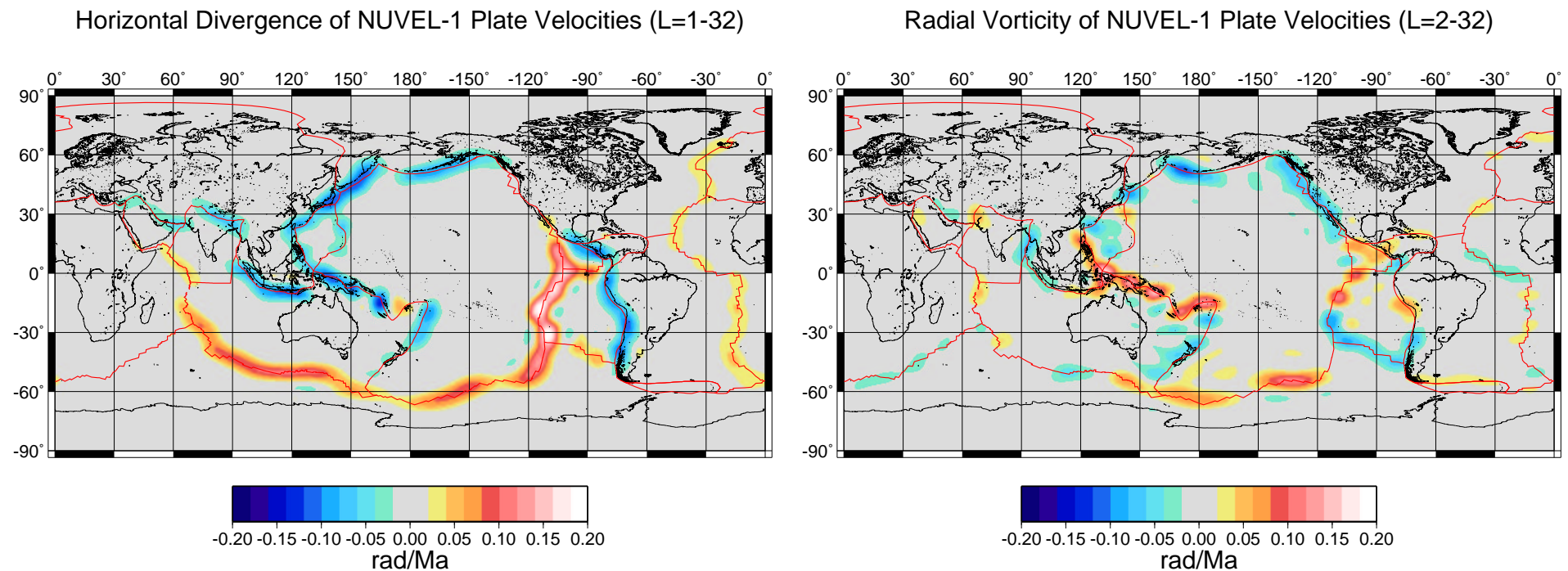


Fig. 5. A two-scalar summary of the observed tectonic plate motions, as represented by NUVEL-1 [DeMets *et al.*, 1990]

2.5.2 mantle-flow Green functions

Parsons & Daly [1983] derived analytic Green functions for buoyancy-induced flow in an *isoviscous* mantle in 2-D Cartesian geometry, ignoring the effects of self gravitation (see equation 14). *Forte & Peltier* [1987] extended the work of *Parsons & Daly* [1983] to 3-D spherical geometry and also included the effects of self gravitation which are important for large-scale flow with horizontal wavelengths comparable to the depth of the mantle. In this section we will review the derivation of the analytic Green functions presented by *Forte & Peltier* [1987].

We will first consider the simplest case of an *isoviscous* mantle, which allows us to simplify the momentum conservation equation (14) as follows:

$$\eta\Delta\mathbf{u} - \nabla P_1 + \rho_o \nabla\phi_1 + \rho_1 \nabla\phi_o = \mathbf{0} \quad (23)$$

Notice, by comparing equations (17) and (13), that we are in effect assuming that the density ρ_o in the hydrostatic configuration is *constant*. We nonetheless allow for the existence of density perturbations ρ_1 in the equation above, because otherwise there would be no buoyancy forces to drive the mantle flow! (This

approximation has been named after *Boussinesq* [1903].)

We will further simplify the momentum equation by assuming that the background gravity field $\mathbf{g}_o = \nabla \phi_o$ may be expressed as:

$$\mathbf{g}_o = -\frac{g_o}{r} \mathbf{r} \quad (24)$$

in which we assume that g_o is *constant*, since the gravitational acceleration is approximately constant in Earth's mantle. (If we insisted on being rigorously consistent with the assumption of constant density ρ_o , then we should calculate the corresponding depth variation of g_o .)

We will now apply the operator, $\mathbf{\Lambda} \cdot \nabla \times$, across the simplified momentum equation (23), and use (24), to obtain the *poloidal flow* equation:

$$\eta \Lambda^2 \Delta^2 p = \Lambda^2 \frac{\rho_1}{r} g_o \quad (25)$$

Similarly, if we apply the operator $\mathbf{\Lambda} \cdot$ across the momentum equation (23), we

obtain the *toroidal flow* equation:

$$\eta\Lambda^2 \Delta q = 0 \quad (26)$$

The derivation of solutions of the partial differential equations of mathematical physics are often simplified by using *Fourier methods*. The basic idea is to use a set of mathematical *basis functions* which provide a *complete* representation of any other function in the particular geometry in which the problem is to be solved (e.g., wave propagation in 1-D Cartesian geometry, or 2-D cylindrical geometry, or 3-D spherical geometry). Consider, for example, the Fourier solution of a 1-D problem involving a function $f(x)$ which is defined over a bounded domain of length $2L$: $-L \leq x \leq +L$. In this situation we may use complex *plane* basis functions as follows:

$$f(x) = \sum_{n=0}^{\infty} f_n e^{\iota k_n x} \text{ where } k_n = \frac{n\pi}{L} \quad (27)$$

in which $\iota = \sqrt{-1}$ and k_n is the *wavenumber* of each basis function. The wavenumber is related to the characteristic *wavelength* of each basis function by

the expression:

$$k_n = \frac{2\pi}{\lambda} \Rightarrow \lambda = \frac{2L}{n} \quad (28)$$

The Fourier basis functions $e^{ik_n x}$ are *eigenfunctions* of the operator d^2/dx^2 :

$$\frac{d^2}{dx^2} e^{ik_n x} = -(k_n)^2 e^{ik_n x} \quad (29)$$

The appropriate basis functions for describing functions on a spherical surface are the *spherical harmonics* $Y_\ell^m(\theta, \varphi)$, where position on the spherical surface is defined by colatitude θ and colongitude φ . We will therefore expand the poloidal and toroidal flow scalar, and the density perturbations, in terms of *spherical harmonic basis functions*, as follows:

$$\left. \begin{aligned} p(r, \theta, \varphi) &= \sum_{\ell=0}^{\infty} \sum_{m=-\ell}^{+\ell} p_\ell^m(r) Y_\ell^m(\theta, \varphi) \\ q(r, \theta, \varphi) &= \sum_{\ell=0}^{\infty} \sum_{m=-\ell}^{+\ell} q_\ell^m(r) Y_\ell^m(\theta, \varphi) \\ \rho_1(r, \theta, \varphi) &= \sum_{\ell=0}^{\infty} \sum_{m=-\ell}^{+\ell} (\rho_1)_\ell^m(r) Y_\ell^m(\theta, \varphi) \end{aligned} \right\} \quad (30)$$

The indices ℓ, m which characterize each spherical harmonic are called the

harmonic degree and *azimuthal order*, respectively. (A useful introduction to spherical harmonic functions may be found in *Jackson* [1975].)

The spherical harmonic functions are eigenfunctions of the horizontal Laplace operator (see equation 21):

$$\frac{\Lambda^2}{r^2} Y_\ell^m(\theta, \varphi) = -\frac{\ell(\ell + 1)}{r^2} Y_\ell^m(\theta, \varphi) \quad (31)$$

Comparing expressions (29) with (31), we note that the 1-D Cartesian wavenumber k_n is equivalent to the 2-D spherical wavenumber $\sqrt{\ell(\ell + 1)}/r$. This formal equivalence allows us to infer the equivalent *horizontal wavelength* λ_ℓ , on a spherical surface of radius r , of a spherical harmonic function $Y_\ell^m(\theta, \varphi)$:

$$\frac{\sqrt{\ell(\ell + 1)}}{r} = \frac{2\pi}{\lambda_\ell}$$

and hence we obtain,

$$\lambda_\ell \approx \frac{2\pi r}{\ell + \frac{1}{2}}, \text{ valid for } \ell \gg 1 \quad (32)$$

Substituting the harmonic expansions (30) into the poloidal and toroidal flow equations (25) and (26), and using (31), we obtain the corresponding spectral flow equations (valid for $\ell \geq 1$):

$$D_\ell^2 p_\ell^m(r) = \frac{1}{\eta} \frac{g_o}{r} (\rho_1)_\ell^m(r) \quad (33)$$

$$D_\ell q_\ell^m(r) = 0 \quad (34)$$

in which D_ℓ is the transformed Laplacian operator Δ :

$$D_\ell = \frac{d^2}{dr^2} + \frac{2}{r} \frac{d}{dr} - \frac{\ell(\ell + 1)}{r^2}$$

The spectral flow equations (33-34) show that lateral density variations can only drive a poloidal flow and that they cannot excite any toroidal flow. This result, obtained under the assumption of an isoviscous mantle, also extends to the more general case of any arbitrary depth-dependent viscosity (will be shown later).

In other words, in the absence of any *lateral viscosity variations*, the mantle flow calculations will be unable to describe the excitation of toroidal flow which is necessary to describe the radial vorticity of the tectonic plate motions.

By virtue of equation (33), the *poloidal-flow Green function* which describes the mantle flow excited by a delta-function density load at any radius r' in the mantle will satisfy the following equation:

$$D_{\ell}^2 p_{\ell}(r, r') = \delta(r - r') \quad (35)$$

The Green function which satisfies (35) can be completely determined by applying appropriate *boundary conditions* at the top and bottom of the mantle and by applying appropriate *matching conditions* at the location of the delta-function load. The Green function will have two domains of definition (see Fig. 6), one for all radii above the delta-function and one for all radii below, as follows:

$$p_{\ell}(r, r') = \begin{cases} (p_1)_{\ell}(r, r') & \text{for } r' < r \leq a \\ (p_2)_{\ell}(r, r') & \text{for } b \leq r < r' \end{cases} \quad (36)$$

Boundary Conditions at $r = a$:

$$\text{zero vertical flow} \Rightarrow (p_1)_\ell(r, r') = 0 \text{ \& free-slip} \Rightarrow \frac{d^2}{dr^2}(p_1)_\ell(r, r') = 0$$



$r=a$ (surface)

1

$$D_\ell^2 (p_1)_\ell(r, r') = 0 \Rightarrow (p_1)_\ell(r, r') = A_1 r^\ell + B_1 \frac{1}{r^{\ell+1}} + C_1 r^{\ell+2} + D_1 \frac{1}{r^{\ell-1}}$$

Matching Conditions at $r = r'$:

$$\frac{d^n}{dr^n}(p_1)_\ell(r, r') = \frac{d^n}{dr^n}(p_2)_\ell(r, r') \quad (n = 0, 1, 2) \quad \& \quad \frac{d^3}{dr^3}(p_1)_\ell(r, r') - \frac{d^3}{dr^3}(p_2)_\ell(r, r') = 1$$



$r=r'$
(Dirac δ -function)

2

$$D_\ell^2 (p_2)_\ell(r, r') = 0 \Rightarrow (p_2)_\ell(r, r') = A_2 r^\ell + B_2 \frac{1}{r^{\ell+1}} + C_2 r^{\ell+2} + D_2 \frac{1}{r^{\ell-1}}$$



$r=b$ (CMB)

Boundary Conditions at $r = b$:

$$\text{zero vertical flow} \Rightarrow (p_2)_\ell(r, r') = 0 \text{ \& free-slip} \Rightarrow \frac{d^2}{dr^2}(p_2)_\ell(r, r') = 0$$

Fig. 6. The isoviscous Green function.

We can show that the poloidal-flow Green function which satisfies all the boundary/matching conditions described in Fig. 6 is:

$$\begin{aligned}
 (p_1)_\ell(r, r') = & \\
 & \frac{a^3}{2(2\ell + 1)(2\ell - 1)} \left(\frac{a}{r'}\right)^{\ell-3} \left[\frac{1 - (r'/b)^{2\ell-1}}{1 - (a/b)^{2\ell-1}} \right] \left[\left(\frac{a}{r}\right)^{\ell-1} - \left(\frac{r}{a}\right)^\ell \right] + \\
 & \frac{a^3}{2(2\ell + 1)(2\ell + 3)} \left(\frac{a}{r'}\right)^{\ell-1} \left[\frac{1 - (r'/b)^{2\ell+3}}{1 - (a/b)^{2\ell+3}} \right] \left[\left(\frac{r}{a}\right)^{\ell+2} - \left(\frac{a}{r}\right)^{\ell+1} \right] \quad (37)
 \end{aligned}$$

and

$$\begin{aligned}
 (p_2)_\ell(r, r') = & \\
 & - \frac{b^3}{2(2\ell + 1)(2\ell - 1)} \left(\frac{b}{r'}\right)^{\ell-3} \left[\frac{1 - (r'/a)^{2\ell-1}}{1 - (b/a)^{2\ell-1}} \right] \left[\left(\frac{b}{r}\right)^{\ell-1} - \left(\frac{r}{b}\right)^\ell \right] \\
 & - \frac{b^3}{2(2\ell + 1)(2\ell + 3)} \left(\frac{b}{r'}\right)^{\ell-1} \left[\frac{1 - (r'/a)^{2\ell+3}}{1 - (b/a)^{2\ell+3}} \right] \left[\left(\frac{r}{b}\right)^{\ell+2} - \left(\frac{b}{r}\right)^{\ell+1} \right] \quad (38)
 \end{aligned}$$

The poloidal-flow Green function (37-38) may now be used to determine the mantle flow for any arbitrary distribution of internal density perturbations as follows:

$$p_{\ell}^m(r) = \frac{g_o}{\eta} \int_b^a \frac{(\rho_1)_{\ell}^m(r')}{r'} p_{\ell}(r, r') dr' \quad (39)$$

$$= \frac{g_o}{\eta} \left[\int_r^a \frac{(\rho_1)_{\ell}^m(r')}{r'} (p_2)_{\ell}(r, r') dr' + \int_b^r \frac{(\rho_1)_{\ell}^m(r')}{r'} (p_1)_{\ell}(r, r') dr' \right] \quad (40)$$

We have so far considered the simple situation of flow in an *isoviscous* mantle. With some additional effort we can also obtain analytic expressions for the flow field in a mantle with a *single viscosity jump* at some arbitrary radius. We again will assume that the viscosity is constant above and below the viscosity discontinuity and therefore the simple isoviscous flow equations (23) can be applied to each layer.

The derivation of the *two-layer poloidal-flow* Green function will thus require the consideration of two cases:

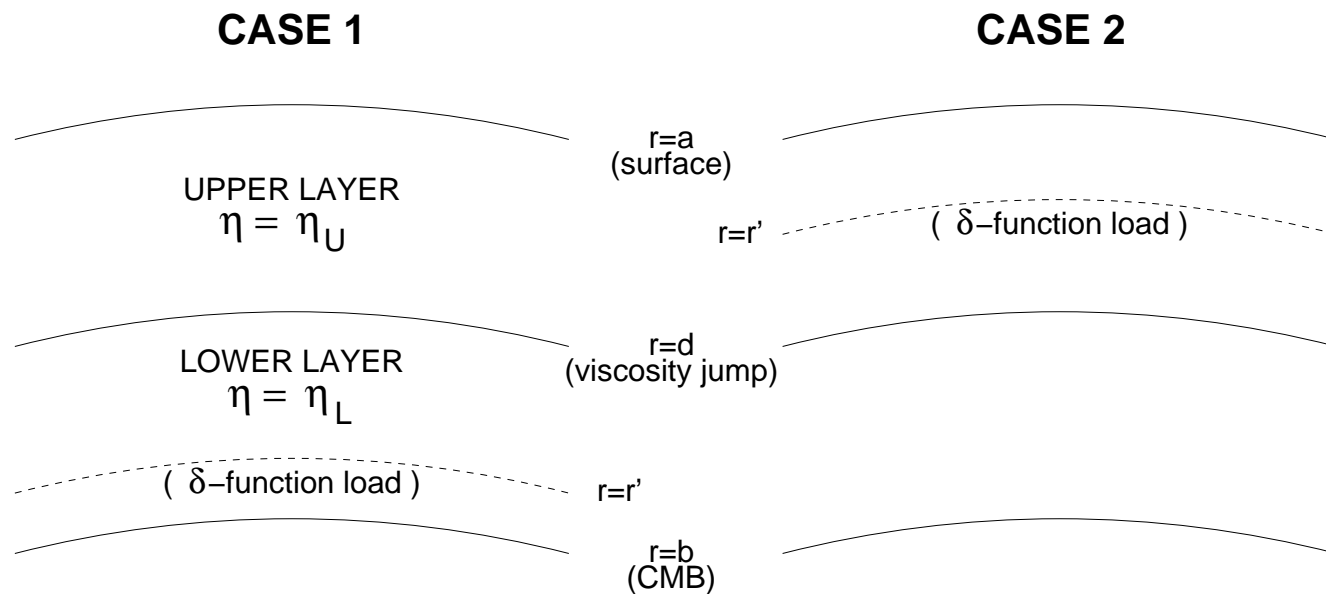


Fig. 7. The two-layer Green function.

The mathematical problem to be solved is:

$$\text{Case 1:} \quad D_{\ell}^2 (p_L)_{\ell}(r, r') = \begin{cases} 0 & d < r < a \\ \delta(r - r') & b < r < d \end{cases} \quad (41)$$

$$\text{Case 2:} \quad D_{\ell}^2 (p_U)_{\ell}(r, r') = \begin{cases} \delta(r - r') & d < r < a \\ 0 & b < r < d \end{cases} \quad (42)$$

Once we obtain the Green functions (41-42), we can readily verify that the poloidal-flow scalar which satisfies equation (33) will be:

$$p_{\ell}^m(r) = \frac{g_o}{\eta_U} \int_d^a \frac{(\rho_1)_{\ell}^m(r')}{r'} (p_U)_{\ell}(r, r') dr' + \frac{g_o}{\eta_L} \int_b^d \frac{(\rho_1)_{\ell}^m(r')}{r'} (p_L)_{\ell}(r, r') dr' \quad (43)$$

in which η_U and η_L are the viscosity of the upper and lower layers, respectively.

A detailed derivation of the two-layer poloidal Green functions (41-42) which

satisfy all appropriate surface (at $r = a, b$) boundary and internal (at $r = d$ and at $r = r'$) matching conditions is too lengthy to present here and may be found in *Forte & Peltier* [1987].

2.5.3 geodynamic kernels for convection-related observables

The poloidal-flow Green functions may be used to derive the *geodynamic kernel functions* which express the mathematical relationship between internal density anomalies and convection-related surface geophysical observables, such as the global *geoid* or *gravity* anomalies, the *horizontal divergence* of the surface plate motions, and the *dynamic topography* at the surface and core-mantle boundary.

The first complete mathematical models of the relationship between geoid anomalies and mantle flow were presented by *Hager* [1984], *Richards & Hager* [1984], and *Ricard et al.* [1984]. A noteworthy study by *Pekeris* [1935] of mantle convection dynamics also provided an investigation of the relationship between mantle convection currents and surface gravity anomalies.

The observed movements of the surface tectonic plates are the most direct manifestation of mantle convection. *Forte & Peltier* [1987] presented the first models which explored the connection between observed plate motions and

tomographically imaged mantle heterogeneity.

The basic physical connection between the geodynamic observables discussed above and the buoyancy-induced mantle flow is illustrated schematically here:

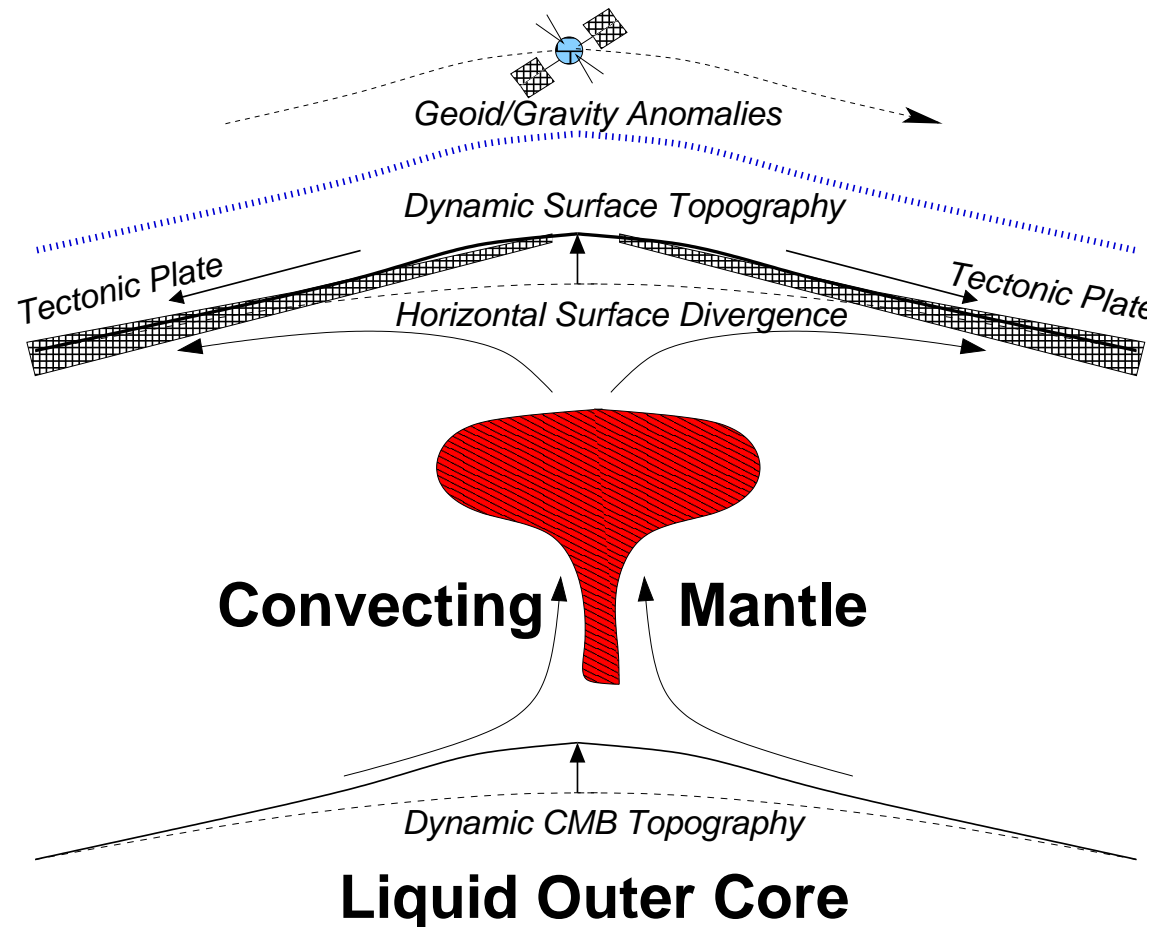


Fig. 8. Geodynamic observables and mantle flow.

The geoid/gravity anomalies will contain a '*direct*' contribution from the driving density perturbations ρ_1 and the '*indirect*' contributions from the flow-induced deflections of all surfaces across which the density changes discontinuously. Density jumps obviously occur at the external boundaries of the mantle (i.e, at $r = a$, the surface, and at $r = b$, the CMB). Significant density jumps also occur internally at phase-change horizons, especially at 400 km and 670 km depth. The density jumps at the surface and at the CMB are by far the largest, therefore in the following we will focus on the gravity perturbations due to deflections of these boundaries.

In the spectral domain, the *internal* gravitational potential perturbations directly due to the mantle density anomalies are given by the classical solution to Poisson's equation (15) [e.g., Jackson, 1975]:

$$(\phi_i)_\ell^m(r) = \frac{4\pi G}{2\ell + 1} \int_b^a r'^2 \frac{r_{<}^\ell}{r_{>}^{\ell+1}} (\rho_1)_\ell^m(r') dr', \quad \text{valid for } b \leq r \leq a, \quad (44)$$

in which $r_{<} = \min(r, r')$ and $r_{>} = \max(r, r')$.

The dynamic deflections of the surface and of the CMB, denoted by δa and δb

respectively, are effectively equivalent to the following sheet-mass density anomalies:

$$\rho_1^a(r) = - [\rho_w - \rho_o(a)] \delta a \delta(r - a) \quad (45)$$

$$\rho_1^b(r) = - [\rho_o(b) - \rho_c] \delta b \delta(r - b) \quad (46)$$

in which ρ_w , ρ_c , $\rho_o(a)$, and $\rho_o(b)$ are the densities of water (assuming a global ocean), the core density just below the CMB, the density at the top of the mantle (i.e. the lithosphere), and the density at the bottom of the mantle, respectively.

The contributions to the geopotential anomalies due to the boundary deflections are readily determined by substituting expressions (45-46) into the potential solution (44), yielding:

$$(\phi_a)_\ell^m(r) = \frac{4\pi G a}{2\ell+1} [\rho_o(a) - \rho_w] \left(\frac{r}{a}\right)^\ell \delta a_\ell^m \quad (47)$$

$$(\phi_b)_\ell^m(r) = \frac{4\pi G b}{2\ell+1} [\rho_c - \rho_o(b)] \left(\frac{b}{r}\right)^{\ell+1} \delta b_\ell^m \quad (48)$$

in which δa_ℓ^m and δb_ℓ^m are the harmonic coefficients of the flow-induced (dynamic) surface and CMB topography, respectively.

Summing all three contributions (44,47,48) to the gravitational potential anomalies yields the total potential perturbation:

$$(\phi_1)_\ell^m(r) = (\phi_i)_\ell^m(r) + (\phi_a)_\ell^m(r) + (\phi_b)_\ell^m(r) \quad (49)$$

In a dynamic, convecting mantle the perturbations to gravitational potential, ϕ_1 , will depend on a rather delicate balance between the direct contribution (ϕ_i) from the driving density anomalies and the contributions from the flow-induced boundary topography at the surface (ϕ_a) and at the CMB (ϕ_b). As we may see from expressions (47-48), for comparable deflections of the surface and CMB, the surface topography signal will dominate the CMB topography signal at the Earth's surface. For the purpose of illustration, we summarize in Fig. 9, below, the gravitational balance between the boundary undulations and internal density anomalies (see *Hager* [1984] for more details):

Is the Total Potential Perturbation $\phi_1 >$ or < 0 ??

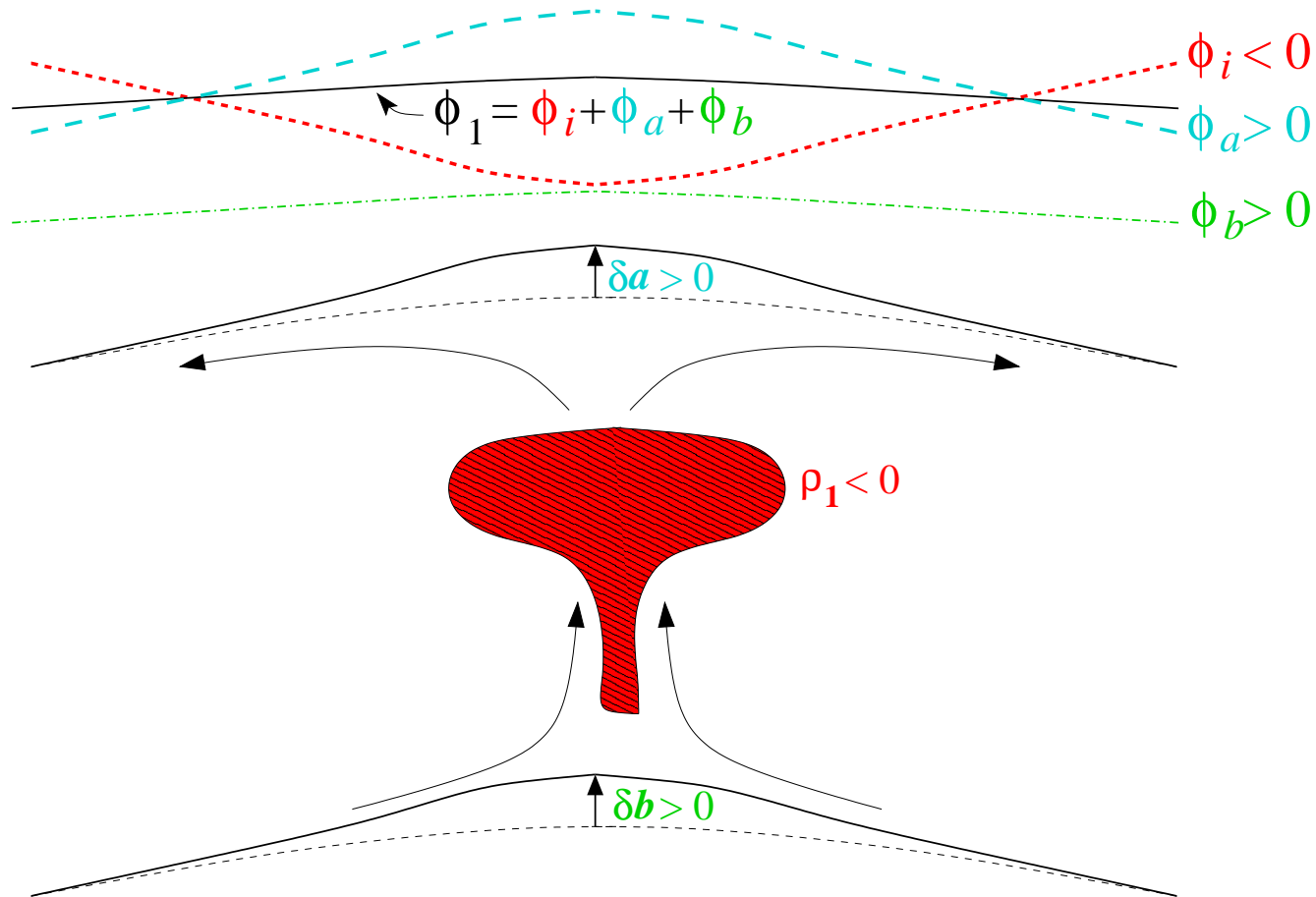


Fig. 9. Balance of contributions to total surface gravitational potential.

The fundamental question raised in Fig. 9 is whether the total gravitational potential perturbation (or equivalently, the geoid anomaly) produced over a low-density anomaly is negative or positive. In an *rigid or elastic* mantle, the

answer is of course *negative*. In a *viscous* mantle the answer depends (mainly) on the amplitude of the dynamic surface deflection generated by the flow induced by the internal density anomaly. If the surface undulation is sufficiently large, its gravitational effect can dominate the opposing contribution directly due to the internal density anomaly. The amplitude of the surface deflections is a strong function of the mantle rheology. This sensitivity may be exploited in efforts to constrain the mantle rheology by studying the observed global geoid anomalies [e.g., *Hager, 1984*].

We may calculate the flow induced deflections of the solid surface (at $r = a$) and of the CMB (at $r = b$), and hence determine the dynamic geoid anomalies, by using the two-layer poloidal Green function (41-42) and using expression (43). (Details of this calculation may be found in *Forte & Peltier [1987]*.) We thus find that the theoretical relationship between the total surface geoid anomalies, denoted by δN , and the internal density anomalies, which takes into account all effects due to the boundary deflections, may be expressed by the following

integral:

$$\delta N_\ell^m = \frac{(\phi_1)_\ell^m(r = a)}{g_o} = \frac{3}{(2\ell + 1)\bar{\rho}} \int_b^a G_\ell(\eta_L/\eta_U; r') (\rho_1)_\ell^m(r') dr' \quad (50)$$

in which the function $G_\ell(\eta_L/\eta_U; r')$ is called the *geoid kernel*. Notice that for a two-layer mantle, the geoid kernels depend only on the *relative viscosity ratio* (η_L/η_U) and not on the absolute values of viscosity in either layer. The observed geoid anomalies will therefore, according to this theory, provide no constraints on absolute mantle viscosity. (Explicit formulas for the two-layer geoid kernels may be found in *Forte & Peltier [1987]*.)

Because of the effects of *self-gravitation* (see equation 14), it turns out that the theoretical calculation of the surface geoid anomalies and of the dynamic topography are coupled and they must be determined simultaneously. The theoretical relationship (see *Forte & Peltier [1987]*) between the dynamic surface

and CMB undulations and the internal density anomalies are:

$$\delta a_\ell^m = \frac{1}{\rho_o - \rho_w} \int_b^a T_\ell(\eta_L/\eta_U; r') (\rho_1)_\ell^m(r') dr' \quad (51)$$

$$\delta b_\ell^m = \frac{1}{\rho_o - \rho_c} \int_b^a B_\ell(\eta_L/\eta_U; r') (\rho_1)_\ell^m(r') dr' \quad (52)$$

We note that, just as for the geoid anomalies (50), the theoretical surface and CMB deflections depend only on the relative viscosity contrast η_L/η_U and not on absolute viscosity.

Finally, we may use the two-layer poloidal Green function to calculate the theoretical relationship between the surface horizontal divergence of the mantle flow and the internal density anomalies:

$$(\nabla_{\mathbf{H}} \cdot \mathbf{u})_\ell^m(r = a) = \frac{g_o}{\eta_U} \int_b^a S_\ell(\eta_L/\eta_U; r') (\rho_1)_\ell^m(r') dr' \quad (53)$$

Here we note that the predicted surface flow is directly sensitive to the absolute values of mantle viscosity. The observed plate motions may therefore be

employed to provide constraints on absolute viscosity in the mantle [e.g., *Forte et al.*, 1991].

In Fig. 10 below we show the theoretical kernel functions for the geodynamic observables described in expressions (50-53).

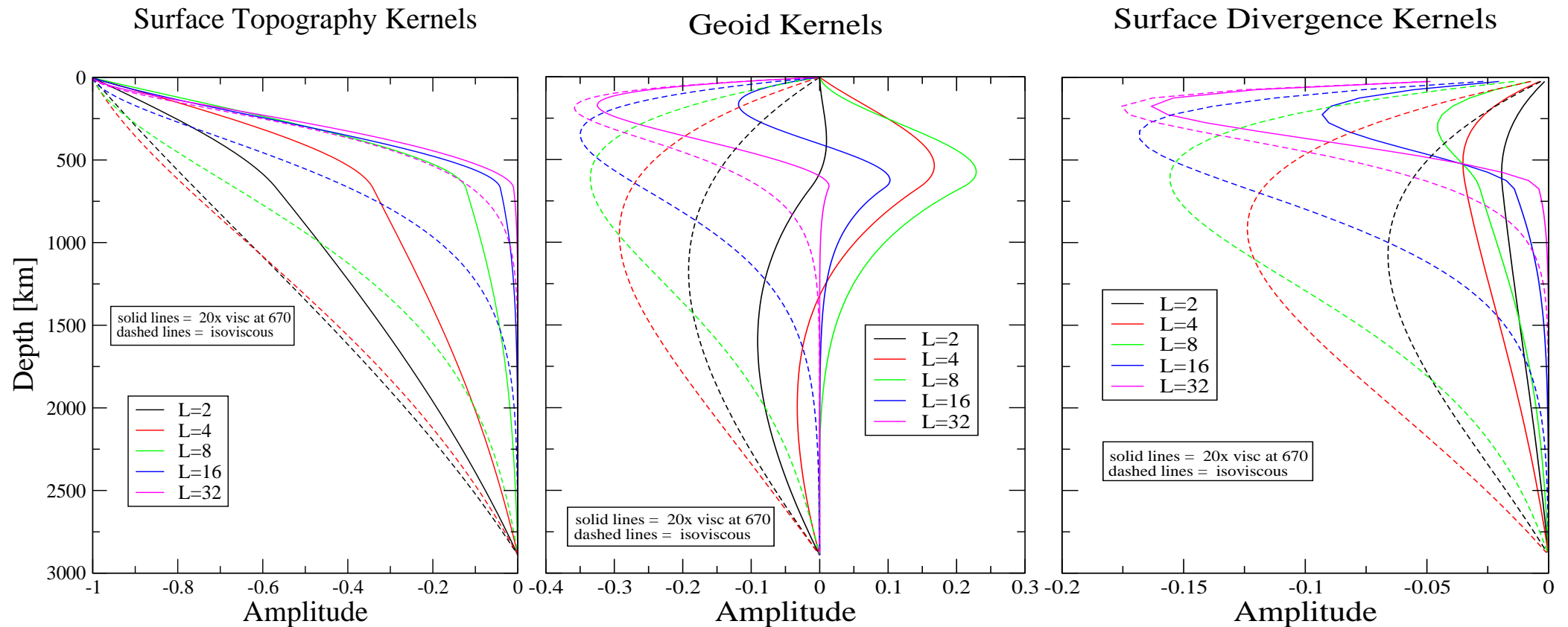


Fig. 10. Geodynamic kernels for an isoviscous mantle and a two-layer mantle with a factor of 20 viscosity jump.

2.6. Numerical solutions for compressible mantle flow

The analytic solutions for an isoviscous and two-layer *incompressible* mantle are useful for investigating the basic physics of flow in 3-D spherical geometry, but they do not take into account several characteristics of the real Earth which are likely to be important.

We know in particular that the density in Earth's mantle, as described for example by PREM [Dziewonski & Anderson, 1981], increases significantly with depth, from a value of 3.38 Mg/m^3 at the top of the mantle to a value of 5.57 Mg/m^3 at the CMB. This implies that a parcel of material which descends from the top of the mantle (e.g., below a subduction zone) will experience a 61% decrease in volume by the time it reaches the CMB. This *finite compressibility* of the mantle is obviously significant and should not be ignored.

In addition it has long been predicted, on the basis of laboratory creep experiments and microphysical models of creep [e.g., Sammis *et al.*, 1977; Ranalli & Fischer, 1984], that the viscosity of the mantle is a strong function of pressure and temperature and therefore will vary significantly with depth.

We also know that the mean radial structure of the mantle exhibits essentially

discontinuous changes in properties at depths of 400 km and 670 km, which may be attributed to an olivine–spinel [e.g., *Ringwood & Major, 1966; Akimoto & Fujisawa, 1968*] and a spinel–post-spinel (perovskite + magnesiowüstite) [e.g., *Ringwood, 1972; Liu, 1976*] phase-change, respectively.

To account for the dynamical effects of these complicated depth-variations of mantle density and rheology, we will discuss in this section a more general, numerical procedure for calculating buoyancy-induced flow in a *compressible* mantle in 3-D spherical geometry. A complete, gravitationally consistent derivation was originally presented by *Forte & Peltier [1991]* and subsequent treatments of 3-D spherical, compressible mantle flow have been presented by *Corrieu et al. [1995]*, *Panasyuk et al. [1996]*, and *Defraigne [1997]*.

2.6.1 covariant tensor form of governing equations

We begin by rewriting the equations for the conservation of mass, momentum, and gravity (13-15), and the constitutive relation (16), in the following *Cartesian*

tensor form:

$$\left. \begin{aligned}
 u_{k,k} &= -\frac{\dot{\rho}_o}{\rho_o} u_r \\
 \sigma_{ij,j} + \rho_o (\phi_1)_{,i} - \rho_1 g_o \hat{\mathbf{r}} &= 0 \\
 \sigma_{ij} &= -P_1 \delta_{ij} + \eta \left(u_{i,j} + u_{j,i} - \frac{2}{3} \delta_{ij} u_{k,k} \right) \\
 (\phi_1)_{,kk} &= -4\pi G \rho_1
 \end{aligned} \right\} \quad (54)$$

in which $\dot{\rho}_o = d\rho_o/dr$, $u_r = \hat{\mathbf{r}} \cdot \mathbf{u}$, and we again used $(\phi_o)_{,i} = -g_o \hat{\mathbf{r}}$. It should also be noted that in these equations we have reverted to the use of the total stress tensor $\boldsymbol{\sigma}$, rather than the deviatoric stress $\boldsymbol{\tau}$ used in (14).

The determination of a solution to the system of tensor equations (54) in spherical geometry may be greatly simplified by using an elegant mathematical technique described by *Phinney & Burridge* [1973]. Following their technique, we begin by introducing a new coordinate system defined by the following *complex*

basis vectors in spherical geometry:

$$\left. \begin{aligned} \hat{e}_- &= \frac{1}{\sqrt{2}} \left(\hat{\vartheta} - \iota \hat{\varphi} \right) \\ \hat{e}_0 &= \hat{r} \\ \hat{e}_+ &= -\frac{1}{\sqrt{2}} \left(\hat{\vartheta} + \iota \hat{\varphi} \right) \end{aligned} \right\} \quad (55)$$

in which $\iota = \sqrt{-1}$, and \hat{r} , $\hat{\vartheta}$, $\hat{\varphi}$ are the unit basis vectors for the standard spherical polar coordinate system.

Following *Phinney & Burridge [1973]*, we will *rotate* all the tensors appearing in the original system (54) into the coordinate system defined by (55), thereby yielding the following *covariant tensor* form of the dynamical equations:

$$\left. \begin{aligned} u^{\alpha,\beta} e_{\alpha\beta} &= -\frac{\dot{\rho}_o}{\rho_o} u^0 \\ \sigma^{\alpha\beta,\gamma} e_{\beta\gamma} + \rho_o (\phi_1)',^\alpha - \rho_1 g_o \delta_0^\alpha &= 0 \\ \sigma^{\alpha\beta} &= -P_1 e^{\alpha\beta} + \eta (u^{\alpha,\beta} + u^{\beta,\alpha}) - \frac{2}{3} \eta (u^{\delta,\gamma} e_{\delta\gamma}) e^{\alpha\beta} \\ (\phi_1)',^{\alpha\beta} e_{\alpha\beta} &= -4\pi G \rho_1 \end{aligned} \right\} \quad (56)$$

in which the Greek indices denote the coordinate directions in system (55) and therefore range over the values $(-1, 0, +1)$. The quantities $e^{\alpha\beta}$, $e_{\alpha\beta}$, and δ_{β}^{α} are the contravariant, covariant, and mixed tensor representations of the Cartesian identity tensor δ_{ij} .

We next represent all quantities in the covariant dynamical equations (56) in terms of expansions over the *generalized spherical harmonic* basis functions $Y_{\ell}^{N m}(\vartheta, \varphi)$, as in *Phinney & Burridge* [1973]:

$$\left. \begin{aligned}
 u^{\alpha}(r, \vartheta, \varphi) &= \sum_{\ell, m} U_{\ell}^{\alpha m}(r) Y_{\ell}^{\alpha m}(\vartheta, \varphi) \\
 \sigma^{\alpha\beta}(r, \vartheta, \varphi) &= \sum_{\ell, m} T_{\ell}^{\alpha\beta m}(r) Y_{\ell}^{(\alpha+\beta) m}(\vartheta, \varphi) \\
 \rho_1(r, \vartheta, \varphi) &= \sum_{\ell, m} (\rho_1)_{\ell}^m(r) Y_{\ell}^{0 m}(\vartheta, \varphi) \\
 P_1(r, \vartheta, \varphi) &= \sum_{\ell, m} (P_1)_{\ell}^m(r) Y_{\ell}^{0 m}(\vartheta, \varphi) \\
 \phi_1(r, \vartheta, \varphi) &= \sum_{\ell, m} (\phi_1)_{\ell}^m(r) Y_{\ell}^{0 m}(\vartheta, \varphi)
 \end{aligned} \right\} \quad (57)$$

We can simplify subsequent numerical computations by *non-dimensionalizing* all

relevant physical variables using the following transformations:

$$\left. \begin{aligned} r &= d r, & g_o(r) &= g_o g(r), & T^{\alpha\beta} &= (\Delta\rho g_o d) T^{\alpha\beta} \\ \eta(r) &= \eta_o \eta(r), & U^\alpha &= \left(\frac{\Delta\rho g_o d^2}{\eta_o} \right) U^\alpha & \phi_1 &= \left(\frac{4\pi G R_o}{2\ell+1} \Delta\rho d \right) \phi_1 \end{aligned} \right\} \quad (58)$$

in which the original variables are on the left of each equation and the non-dimensional variables are on the right. The scaling quantities we have used are defined as follows:

$$\begin{aligned} d &= 2888 \text{ km} && \equiv && \text{radial thickness of mantle} \\ g_o &= 9.82 \text{ m/s}^2 && \equiv && \text{mean surface gravitational acceleration} \\ \Delta\rho &= 0.1 \text{ Mg/m}^3 && \equiv && \text{characteristic subducted slab density anomaly} \\ \eta_o &= 10^{21} \text{ Pa s} && \equiv && \text{Haskell [1935] reference value} \\ R_o &= 6371 \text{ km} && \equiv && \text{mean surface radius of Earth} \end{aligned}$$

Notice, in (58) that we have made a major assumption about mantle *viscosity*, namely that it *varies only with radius*. This assumption will significantly simplify the mathematical manipulations but, as we will see below, it will also result in a

major deficiency with regards to toroidal flow dynamics.

2.6.2 poloidal and toroidal flow equations

We may now substitute the *non-dimensional* form of the expansions (57) into the covariant flow equations (56) and use the *covariant differentiation rules* presented by *Phinney & Burridge* [1973]. (We must also use the orthogonality properties of the generalized spherical harmonics $Y_\ell^{N m}$.) This series of operations finally yields the *separate* systems of equations which govern poloidal and toroidal flow in a compressible mantle. For notational convenience we will henceforth drop the explicit dependence of the flow variables on radius r and on degree and order (ℓ, m) .

The *toroidal* system of equations are obtained by defining the following flow and stress variables:

$$\begin{aligned}U^T &= U^+ - U^- \\T^T &= T^0 + - T^0 -\end{aligned}$$

which yield the following system of coupled, 1st-order, ordinary linear

differential equations:

$$\left. \begin{aligned} \frac{d}{dr} U^T &= \frac{1}{r} U^T + \frac{1}{\eta} T^T \\ \frac{d}{dr} T^T &= \frac{\eta(\ell-1)(\ell+2)}{r^2} U^T - \frac{3}{r} T^T \end{aligned} \right\} \quad (59)$$

We note that the above toroidal flow equations are not affected by the density structure of the mantle, nor by gravity. This is reasonable since toroidal flow has no component in the radial direction. It is also worth noting that the toroidal flow equations have a form identical to the seismological equations which govern infinite-period (zero frequency) toroidal disturbances.

The toroidal flow equations (59) are homogeneous and internal density perturbations ρ_1 cannot excite toroidal flow. This is a consequence of our assumption of a *spherically symmetric viscosity* distribution, and this implies we are unable to provide a dynamically consistent explanation for the origin of toroidal surface (plate) motions. We must introduce asymmetries in mantle rheology (e.g., lateral viscosity variations) in order to excite toroidal flow.

The *poloidal* system of equations are obtained by defining the following *non-dimensionalized* flow and stress variables:

$$\begin{aligned}U^P &= U^+ + U^- \\T^P &= T^{0+} + T^{0-} \\T^0 &= T^{00} + \frac{3}{2\ell+1} \frac{\rho_o}{\bar{\rho}} \phi_1\end{aligned}$$

in which $\bar{\rho} = 5.515 \text{ Mg/m}^3$ is the mean density of the Earth.

These definitions lead to the following coupled system of ordinary, 1st-order, linear differential equations for poloidal flow:

$$\left. \begin{aligned}
\frac{d}{dr} U^0 &= -\frac{1}{r} \left(2 + r \frac{\dot{\rho}_o}{\rho_o} \right) U^0 + \frac{\Omega_1}{r} U^P \\
\frac{d}{dr} U^P &= -\frac{2\Omega_1}{r} U^0 + \frac{1}{r} U^P + \frac{\eta_o}{\eta} T^P \\
\frac{d}{dr} T^0 &= \frac{4}{r^2} \left(3 + r \frac{\dot{\rho}_o}{\rho_o} \right) \frac{\eta}{\eta_o} U^0 - \frac{6\Omega_1}{r^2} \frac{\eta}{\eta_o} U^P + \frac{\Omega_1}{r} T^P \\
&\quad + \frac{3}{2\ell+1} \frac{\dot{\rho}_o}{\rho} \phi_1 + \frac{\rho_1}{\Delta\rho} g(r) \\
\frac{d}{dr} T^P &= -\frac{4\Omega_1}{r^2} \left(3 + r \frac{\dot{\rho}_o}{\rho_o} \right) \frac{\eta}{\eta_o} U^0 + \frac{2}{r^2} (\Omega_2^2 + 3\Omega_1^2) \frac{\eta}{\eta_o} U^P \\
&\quad - \frac{2\Omega_1}{r} T^0 - \frac{3}{r} T^P \\
\frac{d}{dr} \phi_1 &= g_1 \\
\frac{d}{dr} g_1 &= -\frac{2}{r} g_1 + \frac{\ell(\ell+1)}{r^2} \phi_1 - (2\ell+1) \left(\frac{d}{R_o} \right) \frac{\rho_1}{\Delta\rho}
\end{aligned} \right\} \quad (60)$$

in which $\Omega_1 = [\ell(\ell+1)/2]^{1/2}$ and $\Omega_2 = [(\ell-1)(\ell+2)/2]^{1/2}$.

In the poloidal equations (60) we note the presence of the *self-gravitational loading* term $\dot{\rho}_o \phi_1$ which describes the gravitational interaction of the perturbed potential with the background, hydrostatic density structure of the mantle. This term, in effect, describes ‘geoidal’ undulations inside the mantle and it requires that the solution for the flow variables (U^0, U^P, T^0, T^P) and the perturbed

gravity field must be determined simultaneously. For an *incompressible* mantle, where $\rho_o = 0$, the four flow equations in (60) governing (U^0, U^P, T^0, T^P) may be solved independently of the two gravity equations governing (ϕ_1, g_1) .

The poloidal-flow system of equations (60) may be compactly written in matrix form as follows:

$$\frac{d}{dr} \mathbf{v}(r) = \mathbf{M}(r) \mathbf{v}(r) + \mathbf{a}(r) \quad (61)$$

where

$$\mathbf{v}(r) = \begin{pmatrix} U^0(r) \\ U^P(r) \\ T^0(r) \\ T^P(r) \\ \phi_1(r) \\ g_1(r) \end{pmatrix} \quad \mathbf{a}(r) = \begin{pmatrix} 0 \\ 0 \\ g(r) \\ 0 \\ 0 \\ -(2\ell + 1) \left(\frac{d}{R_o} \right) \end{pmatrix} \frac{\rho_1(r)}{\Delta\rho} \quad (62)$$

and

$$\mathbf{M}(r) = \begin{pmatrix} -\frac{[2+r(\dot{\rho}_o/\rho_o)]}{r} & \frac{\Omega_1}{r} & 0 & 0 & 0 & 0 \\ -\frac{2\Omega_1}{r} & \frac{1}{r} & 0 & \frac{\eta_o}{\eta} & 0 & 0 \\ \frac{4[3+r(\dot{\rho}_o/\rho_o)]}{r^2} \frac{\eta}{\eta_o} & -\frac{6\Omega_1}{r^2} \frac{\eta}{\eta_o} & 0 & \frac{\Omega_1}{r} & \frac{3}{2\ell+1} \frac{\dot{\rho}_o}{\bar{\rho}} & 0 \\ -\frac{4\Omega_1[3+r(\dot{\rho}_o/\rho_o)]}{r^2} \frac{\eta}{\eta_o} & \frac{2[\Omega_2^2+3\Omega_1^2]}{r^2} \frac{\eta}{\eta_o} & -\frac{2\Omega_1}{r} & -\frac{3}{r} & 0 & 0 \\ 0 & 0 & 0 & 0 & 0 & 1 \\ 0 & 0 & 0 & 0 & \frac{\ell(\ell+1)}{r^2} & -\frac{2}{r} \end{pmatrix} \quad (63)$$

2.6.3 poloidal-flow Green function

Our objective is to solve the flow system (61) for a delta-function density load at an arbitrary radial position in the mantle. We will thereby obtain the compressible-flow Green function for a mantle with any given radial density and viscosity profiles.

We will first determine that internal matching conditions which must be satisfied

at the location of the delta-function density load:

$$\frac{\rho_1(r)}{\Delta\rho} = \delta(r - r') \quad (64)$$

Expression (64) is substituted into the system of equations (60) and we integrate each of the equations from $r'_- = r' - \epsilon$ to $r'_+ = r' + \epsilon$, taking the limit $\epsilon \rightarrow 0$. We must pay special attention to the possibility that the location $r = r'$ of the delta-function load might also coincide with the mean radial position $r = r_o$ of a material boundary in the mantle (e.g., a phase-change horizon) where the density changes discontinuously, such that:

$$\left(\frac{d\rho_o}{dr} \right)_{r=r_o} = [\rho_o(r_o^+) - \rho_o(r_o^-)] \delta(r - r_o) \quad (65)$$

where $\rho_o(r_o^+)$ and $\rho_o(r_o^-)$ are the mantle density immediately above and below the material boundary, respectively.

The matching condition for the radial velocity component U^0 is obtained by

integrating the first equation in the system (60):

$$U^0(r'_+) - U^0(r'_-) = - \left[\frac{\rho_o(r'_+) - \rho_o(r'_-)}{\langle \rho_o(r') \rangle} \right] \langle U^0(r') \rangle \quad (66)$$

where the notation $\langle f(r') \rangle$ will henceforth represent the average of a discontinuous quantity:

$$\langle f(r') \rangle = \frac{1}{2} [f(r'_+) + f(r'_-)] \quad (67)$$

Combining expressions (66) and (67) we finally obtain the desired radial velocity matching condition:

$$\rho_o(r'_+)U^0(r'_+) = \rho_o(r'_-)U^0(r'_-) \quad (68)$$

The matching condition for the tangential velocity component U^P is obtained by integrating the second equation in (60):

$$U^P(r'_+) - U^P(r'_-) = 0 \Leftrightarrow U^P(r'_+) = U^P(r'_-) \quad (69)$$

The matching condition for the radial stress tensor component T^0 is obtained by integrating the third equation in (60):

$$T^0(r'_+) - T^0(r'_-) = \Delta_u(r') + \frac{3}{2\ell + 1} \left[\frac{\rho_o(r'_+) - \rho_o(r'_-)}{\bar{\rho}} \right] \langle \phi_1(r') \rangle + g(r') \quad (70)$$

where

$$\Delta_u(r') = \frac{4}{r'} \left[\frac{\rho_o(r'_+) - \rho_o(r'_-)}{\langle \rho_o(r') \rangle} \right] \frac{\langle \eta(r') \rangle}{\eta_o} \langle U^0(r') \rangle$$

$$[\text{using (67 \& (66))}] \Leftrightarrow \Delta_u(r') = -\frac{2}{r'} \left(\frac{\eta(r'_+) + \eta(r'_-)}{\eta_o} \right) [U^0(r'_+) - U^0(r'_-)] \quad (71)$$

The matching condition for the tangential stress component T^P is obtained by integrating the fourth equation in (60):

$$T^P(r'_+) - T^P(r'_-) = -\Omega_1 \Delta_u(r') \quad (72)$$

where $\Delta_u(r')$ is defined in (71). The matching conditions for the perturbed

gravitational potential and acceleration are obtained by integrating the last two equations in (60):

$$\phi_1(r'_+) - \phi_1(r'_-) = 0 \Leftrightarrow \phi_1(r'_+) = \phi_1(r'_-) \quad (73)$$

$$g_1(r'_+) - g_1(r'_-) = -(2\ell + 1) \left(\frac{d}{R_o} \right) \quad (74)$$

We now have a full set of matching conditions at the location ($r = r'$) of the delta-function density load. The corresponding Green function will also require the specification of a complete set of *internal matching conditions at internal material boundaries* (e.g., at phase-change horizons or at chemical boundaries) and the specification of *boundary conditions* at the surface ($r = a$) and at the CMB ($r = b$). We consider each of these in turn.

2.6.4 matching conditions at internal boundaries

We consider here the matching conditions which must be satisfied when characteristic properties of the mantle, especially density, viscosity and chemical composition, change very rapidly across phase-change or chemical horizons in

the mantle. We will approximate such rapid vertical changes as mathematical discontinuities. We will first denote the mean (i.e. horizontally averaged) location of the boundary as $r = r_i$ and we will allow for geographic variations in the radial location (i.e., deflections) of the boundary as follows:

$$r = r_i + \delta r_i, \quad \text{where we assume} \quad \left| \frac{\delta r_i}{r_i} \right| \ll 1 \quad (75)$$

As we have already seen in expression (65), a discontinuous change in density across the internal boundary implies that:

$$\left(\frac{d\rho_o}{dr} \right)_{r=r_i} = \left[\rho_o(r_i^+) - \rho_o(r_i^-) \right] \delta(r - r_i) \quad (76)$$

As per equations (45-46), we may approximate the density perturbation due to the boundary deflection δr_i in terms of the following sheet-mass anomaly:

$$\delta\rho_i = - \left(\frac{d\rho_o}{dr} \right)_{r=r_i} \delta r_i = - \left[\rho_o(r_i^+) - \rho_o(r_i^-) \right] \delta r_i \delta(r - r_i) \quad (77)$$

A comparison of expressions (64) and (77) shows that an internal boundary deflection effectively gives rise to a delta-function load, such that the corresponding density perturbation is, in non-dimensional terms:

$$\frac{\rho_1(r)}{\Delta\rho} = -\frac{[\rho_o(r_i^+) - \rho_o(r_i^-)]}{\Delta\rho} \frac{\delta r_i}{d} \delta(r - r_i) \quad (78)$$

The complete mathematical equivalence between expressions (65) & (76), on the one hand, and between (64) & (78) on the other, implies that we can treat the mechanical effects of a deflected phase-change boundary in an identical way as buoyancy sources elsewhere in the mantle. The only modification is in the case of matching conditions (70) and (74) which, for a phase-change, become:

$$T^0(r_i^+) - T^0(r_i^-) = \Delta_u(r_i) + \frac{3}{2\ell + 1} \left[\frac{\rho_o(r_i^+) - \rho_o(r_i^-)}{\bar{\rho}} \right] \phi_1(r_i) - \frac{[\rho_o(r_i^+) - \rho_o(r_i^-)]}{\Delta\rho} \frac{\delta r_i}{d} g(r_i) \quad (79)$$

and

$$g_1(r_i^+) - g_1(r_i^-) = (2\ell + 1) \left(\frac{d}{R_o} \right) \frac{[\rho_o(r_i^+) - \rho_o(r_i^-)]}{\Delta\rho} \frac{\delta r_i}{d} \quad (80)$$

All other matching conditions (i.e., 68, 69, 72, 73) apply identically to the case of the deflected phase-change boundary.

If we assume that the internal boundary corresponds to a *chemical discontinuity*, then we must impose a zero radial velocity condition (an identical condition is also applied at the solid surface and at the CMB):

$$U^0(r_i^+) = 0 = U^0(r_i^-)$$

This boundary condition must however be supplemented by an *additional matching condition*, concerning the boundary topography δr_i which was not required in the case of the phase-change problem. A special treatment is required for the problem of a chemical discontinuity and we will defer this to a later section.

2.6.5 boundary conditions at the solid surface

We will assume, as in *Forte & Peltier* [1991] that our spherically symmetric, hydrostatic reference Earth model is overlain by a global ocean layer which is 3 km thick, as in PREM. We also combine PREM's crust and seismic lithosphere (LID) into a single lithospheric layer which contains the same total mass as the two PREM layers. PREM's crust and seismic lithosphere are combined into a single mechanical layer because it is assumed that both will deform and move together in response to the buoyancy driven flow in the mantle.

The top surface of the combined lithosphere is located at radius $r = a = 6368 \text{ km}$ and the base is located at radius 6291 km (i.e., at a depth of 80 km below the surface of the global ocean layer). This redefined lithosphere has mass density of 3.2 Mg/m^3 .

In view of the very complicated mechanical and rheological properties of the crust and underlying lithosphere, it is clear that the simple theory we have developed which assumes a purely depth-dependent viscosity cannot provide an adequate representation of the near-surface dynamics. We will consider these issues in a subsequent lecture, which will deal with tectonic plates and lateral

viscosity variations. In the meantime, we will consider here two different boundary conditions of interest at the solid-surface: *free-slip* and *no-slip*.

There can be no flow across the bounding surface $r = a$ and therefore:

$$U^0(a^-) = \begin{cases} 0 & \text{for } \textit{free-slip} \\ 0 & \text{for } \textit{no-slip} \end{cases} \quad (81)$$

where a^- denotes the radial location $r = a - \epsilon$. In the global ocean layer which overlies the lithosphere we also assume zero radial flow at the boundary location:

$$U^0(a^+) = 0 \quad (82)$$

The condition for the surface tangential flow $U^P(a^-)$ in the lithosphere is:

$$U^P(a^-) = \begin{cases} U^P(a^-) & \text{to be determined, for } \textit{free-slip} \\ 0 & \text{for } \textit{no-slip} \end{cases} \quad (83)$$

We can apply the radial stress T^0 matching condition in (79) to the deformed surface boundary which, by virtue of conditions (81-82), becomes:

$$T^0(a^-) - T^0(a^+) = \frac{3}{2\ell + 1} \left[\frac{\Delta\rho_a}{\bar{\rho}} \right] \phi_1(a^-) - \left[\frac{\Delta\rho_a}{\Delta\rho} \right] \frac{\delta a}{d} g(a) \quad (84)$$

where we have defined the density jump across the solid surface:

$$\Delta\rho_a = \rho_o(a^-) - \rho_o(a^+) = 3.2 - 1.0 \text{ Mg}/m^3 = 2.2 \text{ Mg}/m^3 \quad (85)$$

and where we have also invoked the universally valid condition (73) for the vertical continuity of the perturbed gravitational potential.

We need to establish in (84) the value of $T^0(a^+)$ which corresponds to the radial stress in the global ocean layer. If we assume that the viscosity in the global ocean layer is negligible (i.e., $\eta/\eta_o \rightarrow 0$), then the 2nd equation in system (60) yields:

$$T^P(r) = 0, \text{ throughout the ocean layer} \quad (86)$$

and therefore, by virtue of this result, the 4th equation in system (60) yields:

$$T^0(r) = 0, \text{ throughout the ocean layer} \quad (87)$$

Substituting result (87) into expression (84) yields the desired radial-stress boundary condition at the surface:

$$T^0(a^-) = \frac{3}{2\ell + 1} \left[\frac{\Delta\rho_a}{\bar{\rho}} \right] \phi_1(a^-) - \left[\frac{\Delta\rho_a}{\Delta\rho} \right] \frac{\delta a}{d} g(a) \text{ valid for free-slip \& no-slip} \quad (88)$$

in which δa is the vertical deflection of the solid surface (i.e., *dynamic surface topography*).

The condition for the surface tangential stress $T^P(a^-)$ is as follows:

$$T^P(a^-) = \begin{cases} 0 & \text{for free-slip} \\ T^P(a^-) & \text{to be determined, for no-slip} \end{cases} \quad (89)$$

By virtue of the general result (73), and using result (80), the surface matching

conditions for the perturbed gravitational potential and acceleration are:

$$\phi_1(a^-) = \phi_1(a^+) \quad (90)$$

$$g_1(a^-) = g_1(a^+) + (2\ell + 1) \left(\frac{d}{R_o} \right) \left[\frac{\Delta\rho_a}{\Delta\rho} \right] \frac{\delta a}{d} \quad (91)$$

The ocean-layer potential and gravity fields $\phi_1(a^+)$ and $g_1(a^+)$, respectively, are not independent of each other and, as shown in *Forte & Peltier* [1991], they are both related to the perturbed potential at the *surface of the global ocean layer*, $\phi_1(r = R_o)$:

$$\phi_1(a^+) = P_\ell \phi_1(R_o) \quad (92)$$

$$g_1(a^+) = G_\ell \phi_1(R_o) \quad (93)$$

in which the ocean-layer response functions P_ℓ and G_ℓ are as follows:

$$P_\ell = \left(\frac{R_o}{a}\right)^{\ell+1} - \frac{3}{2\ell+1} \frac{\rho_w}{\bar{\rho}} \left[\left(\frac{R_o}{a}\right)^{\ell+2} - \left(\frac{a}{R_o}\right)^{\ell-1} \right] \quad (94)$$

$$G_\ell = -(\ell+1) \frac{d}{R_o} \left(\frac{R_o}{a}\right)^{\ell+2} + \frac{3}{2\ell+1} \frac{\rho_w}{\bar{\rho}} \frac{d}{R_o} \left[(\ell+1) \left(\frac{R_o}{a}\right)^{\ell+3} + \ell \left(\frac{a}{R_o}\right)^{\ell-2} \right] \quad (95)$$

in which $\rho_w \equiv \rho(a^+) = 1 \text{ Mg/m}^3$ is the density of the global ocean layer.

Substitution of results (92-93) into expressions (90-91) yields the complete surface boundary conditions for the gravitational variables:

$$\phi_1(a^-) = P_\ell \phi_1(R_o), \text{ valid for } \textit{free-slip} \ \& \ \textit{no-slip} \quad (96)$$

$$g_1(a^-) = G_\ell \phi_1(R_o) + (2\ell+1) \left(\frac{d}{R_o}\right) \left[\frac{\Delta\rho_a}{\Delta\rho} \right] \frac{\delta a}{d}, \text{ valid for } \textit{free-slip} \ \& \ \textit{no-slip} \quad (97)$$

It should be noted that expression (96) should also be substituted into the radial stress condition (88).

We can now summarize the complete set of free-slip and no-slip surface boundary conditions, in terms of the poloidal-flow vector $\mathbf{v}(r = a)$ defined in expression (62):

Free-slip:

$$\mathbf{v}(a^-) = U^P(a^-) \mathbf{y}_1 + \phi_1(R_o) \mathbf{y}_2 + \frac{\Delta\rho_a}{\Delta\rho} \frac{\delta a}{d} \mathbf{y}_3 \quad (98)$$

in which the surface basis vectors are:

$$\mathbf{y}_1 = \begin{pmatrix} 0 \\ 1 \\ 0 \\ 0 \\ 0 \\ 0 \end{pmatrix} \quad \mathbf{y}_2 = \begin{pmatrix} 0 \\ 0 \\ \frac{3}{2\ell+1} \frac{\Delta\rho_a}{\bar{\rho}} P_\ell \\ 0 \\ P_\ell \\ G_\ell \end{pmatrix} \quad \mathbf{y}_3 = \begin{pmatrix} 0 \\ 0 \\ -g(a) \\ 0 \\ 0 \\ (2\ell + 1) \left(\frac{d}{R_o} \right) \end{pmatrix} \quad (99)$$

No-slip:

$$\mathbf{v}(a^-) = T^P(a^-) \mathbf{y}'_1 + \phi_1(R_o) \mathbf{y}_2 + \frac{\Delta\rho_a}{\Delta\rho} \frac{\delta a}{d} \mathbf{y}_3 \quad (100)$$

in which the surface basis vectors are:

$$\mathbf{y}'_1 = \begin{pmatrix} 0 \\ 0 \\ 0 \\ 1 \\ 0 \\ 0 \end{pmatrix} \quad \text{and } \mathbf{y}_2, \mathbf{y}_3 \text{ are defined in (99)} \quad (101)$$

2.6.6 boundary conditions at the CMB

The derivation of the boundary conditions which apply at $r = b$, the CMB, is almost identical to the derivation for the surface boundary conditions ($r = a$), in the preceding section. The only difference concerns the application of gravitational matching conditions at $r = b$, since we must now deal with the interaction between a deformed CMB and a *compressible, hydrostatic* core.

A detailed treatment of the gravitational perturbations maintained in a hydrostatic core is presented in *Forte & Peltier* [1991], where it is shown that perturbed gravitational acceleration at the top of the core (i.e., immediately below the CMB) is determined by the perturbed potential at the bottom of the mantle (i.e., immediately above the CMB), as follows:

$$g_1(b^-) = R_\ell \phi_1(b^+)$$

where b^- denotes the radial location $r = b - \epsilon$ (i.e., bottom side of the CMB) and b^+ denotes $r = b + \epsilon$ (i.e., top side of the CMB). R_ℓ is a numerically determined coefficient which is obtained on the basis of the compressible density profile throughout the core [*Forte & Peltier*, 1991].

As shown in *Forte & Peltier* [1991], the complete set of free-slip, CMB boundary conditions in terms of the poloidal-flow vector $\mathbf{v}(r = b)$ defined in expression (62) is:

$$\mathbf{v}(b^+) = U^P(b^+) \mathbf{x}_1 + \phi_1(b^+) \mathbf{x}_2 + \frac{\Delta\rho_b}{\Delta\rho} \frac{\delta b}{d} \mathbf{x}_3 \quad (102)$$

in which the CMB basis vectors are:

$$\mathbf{x}_1 = \begin{pmatrix} 0 \\ 1 \\ 0 \\ 0 \\ 0 \\ 0 \end{pmatrix} \quad \mathbf{x}_2 = \begin{pmatrix} 0 \\ 0 \\ \frac{3}{2\ell+1} \frac{\Delta\rho_b}{\bar{\rho}} \\ 0 \\ 1 \\ R_\ell \end{pmatrix} \quad \mathbf{x}_3 = \begin{pmatrix} 0 \\ 0 \\ -g(b) \\ 0 \\ 0 \\ (2\ell + 1) \left(\frac{d}{R_o} \right) \end{pmatrix} \quad (103)$$

in which $\Delta\rho_b = \rho_o(b^+) - \rho(b^-) = -4.434 \text{ Mg}/\text{m}^3$ is the density jump across the CMB and δb is the deflection (i.e., dynamic topography) of the CMB.

2.6.7 numerical calculation of compressible-flow geodynamic kernels

For a mantle with complex density (e.g., as in PREM) and viscosity profiles, the poloidal-flow system of equations (61) must be integrated numerically. When $r \neq r'$, this linear system of equations is homogeneous:

$$\frac{d}{dr} \mathbf{v}(r) = \mathbf{M}(r) \mathbf{v}(r), \text{ (when } r \neq r') \quad (104)$$

We can propagate each of the surface boundary vectors \mathbf{y}_i ($i = 1, 2, 3$) in (99) or (101), by numerically integrating (104) from the surface ($r = a^-$) *downward* to $r = r'$, stopping along the way at all internal material boundaries ($r = r_i$) where we apply the internal matching conditions described previously (*section 2.6.4*). We can similarly propagate each of the CMB basis vectors \mathbf{x}_i ($i = 1, 2, 3$) in (103) from the CMB ($r = b^+$) *upward* to $r = r'$. The basic procedure is summarized schematically in Fig. 11 below.

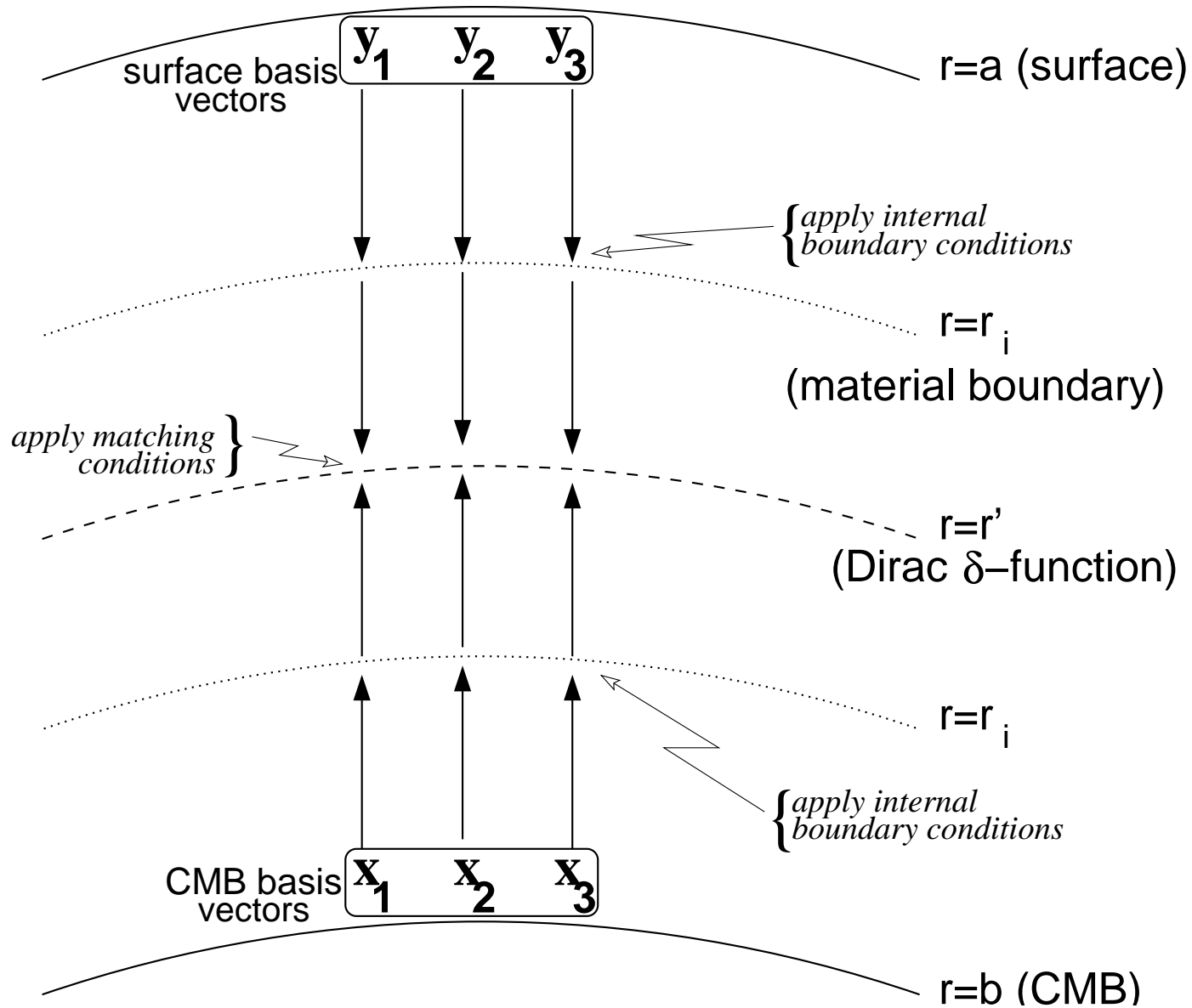


Fig. 11. Numerical integration of the poloidal-flow system of equations in (61)

At the location $r = r'$ of the delta-function load we apply the matching conditions (68, 69, 70, 72, 73, 74). For each of these matching conditions we employ the corresponding components of the poloidal-flow vectors $\mathbf{v}(r'_+)$ and $\mathbf{v}(r'_-)$, which are obtained from expressions (98), (100) and (102):

$$\mathbf{v}(r'_+) = \left\{ \begin{array}{l} U^P(a^-) \mathbf{y}_1(r'_+) \\ T^P(a^-) \mathbf{y}'_1(r'_+) \end{array} \right\} + \phi_1(R_o) \mathbf{y}_2(r'_+) + \frac{\Delta\rho_a}{\Delta\rho} \frac{\delta a}{d} \mathbf{y}_3(r'_+) \quad (105)$$

and

$$\mathbf{v}(r'_-) = U^P(b^+) \mathbf{x}_1(r'_-) + \phi_1(b^+) \mathbf{x}_2(r'_-) + \frac{\Delta\rho_b}{\Delta\rho} \frac{\delta b}{d} \mathbf{x}_3(r'_-) \quad (106)$$

in which the surface and CMB basis vectors, $\mathbf{y}_i(r'_+)$ and $\mathbf{x}_i(r'_-)$, have been obtained by the numerical integration of (104), as outlined above. The application of the six matching conditions then yields the following system of

equations:

$$\mathbf{A} \mathbf{b} = \boldsymbol{\delta} \quad (107)$$

in which

$$\mathbf{b} = \begin{pmatrix} U^P(a^-) \text{ or } T^P(a^-) \\ \phi_1(R_o) \\ \frac{\Delta\rho_a}{\Delta\rho} \frac{\delta a}{d} \\ U^P(b^+) \\ \phi_1(b^+) \\ \frac{\Delta\rho_b}{\Delta\rho} \frac{\delta b}{d} \end{pmatrix} \quad \text{and} \quad \boldsymbol{\delta} = \begin{pmatrix} 0 \\ 0 \\ g(r') \\ 0 \\ 0 \\ -(2\ell + 1) \frac{d}{R_o} \end{pmatrix} \quad (108)$$

Each row of the 6×6 matrix \mathbf{A} , in (107), involves elements taken from the corresponding rows of the basis vectors $\mathbf{y}_i(r'_+)$ and $\mathbf{x}_i(r'_-)$ in (105-106).

For any given position $r = r'$ of the delta-function load we obtain a system of equations given by (107) which can be simply solved to find the unknown vector \mathbf{b} . We can show on the basis of the non-dimensionalization scheme (58), that the elements of \mathbf{b} will correspond to values (at $r = r'$) of different geodynamic

kernel functions:

$$\begin{aligned} \phi_1(R_o) &\Leftrightarrow \text{geoid kernel: } G_\ell(r') \text{ in (50)} \\ \frac{\Delta\rho_a}{\Delta\rho} \frac{\delta a}{d} &\Leftrightarrow \text{surface topography kernel: } T_\ell(r') \text{ in (51)} \\ \frac{\Delta\rho_b}{\Delta\rho} \frac{\delta b}{d} &\Leftrightarrow \text{CMB topography kernel: } B_\ell(r') \text{ in (52)} \\ -\frac{d}{a} \Omega_1 U^P(a^-) &\Leftrightarrow \text{surface divergence kernel: } S_\ell(r') \text{ in (53)} \end{aligned}$$

3. Modelling Convection-Related Surface Observables

In this section we will briefly consider some numerical predictions which can be obtained on the basis of the compressible-flow theory of the mantle, presented above in section 2.6. The fundamental ingredient required in the flow calculations is knowledge of the radial density structure of the hydrostatic Earth and the depth dependence of the mantle viscosity. The radial density profile given by PREM [*Dziewonski & Anderson, 1981*] will be employed in all calculations presented below.

Geodynamic inferences of mantle viscosity traditionally come from two distinct families of data which are (with rare exceptions) treated separately: (1) post-glacial rebound data [e.g., *Mitrovica, 1996*] and (2) surface data associated with mantle convection [e.g., *Hager & Clayton, 1989*]. A (somewhat dated) review of published geophysical inferences of mantle viscosity may be found in *King [1995]*.

3.1. Geodynamic kernels for a compressible mantle

For the purposes of this discussion we will focus on the viscosity inferences obtained by *Forte & Mitrovica* [1996] and *Mitrovica & Forte* [1997], who performed the first *simultaneous inversions* of both the post-glacial rebound and mantle convection data sets. Despite the very different time and spatial scales over which these processes operate, they found that it was possible to explain both families of data with a single viscosity profile. We will consider here one of the profiles obtained by *Mitrovica & Forte* [1997], called 'MF2', shown below in Fig. 12.

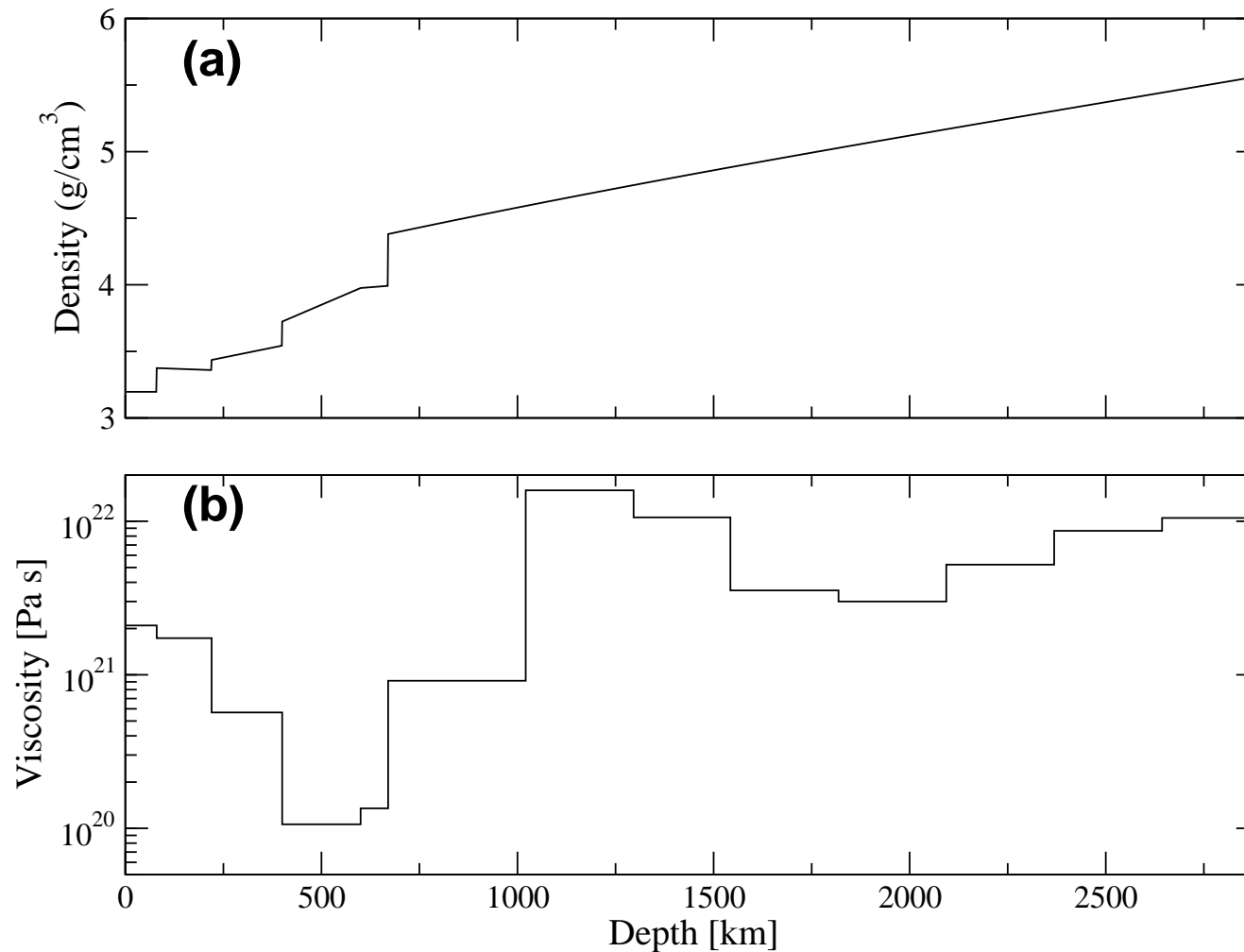


Fig. 12. (a) PREM density profile (b) Radial viscosity profile – model MF2 [Mitrovica & Forte, 1997].

The geodynamic kernels calculated using the density and viscosity profiles in Fig. 12, are compared to *incompressible*-flow predictions in Fig. 13 below.

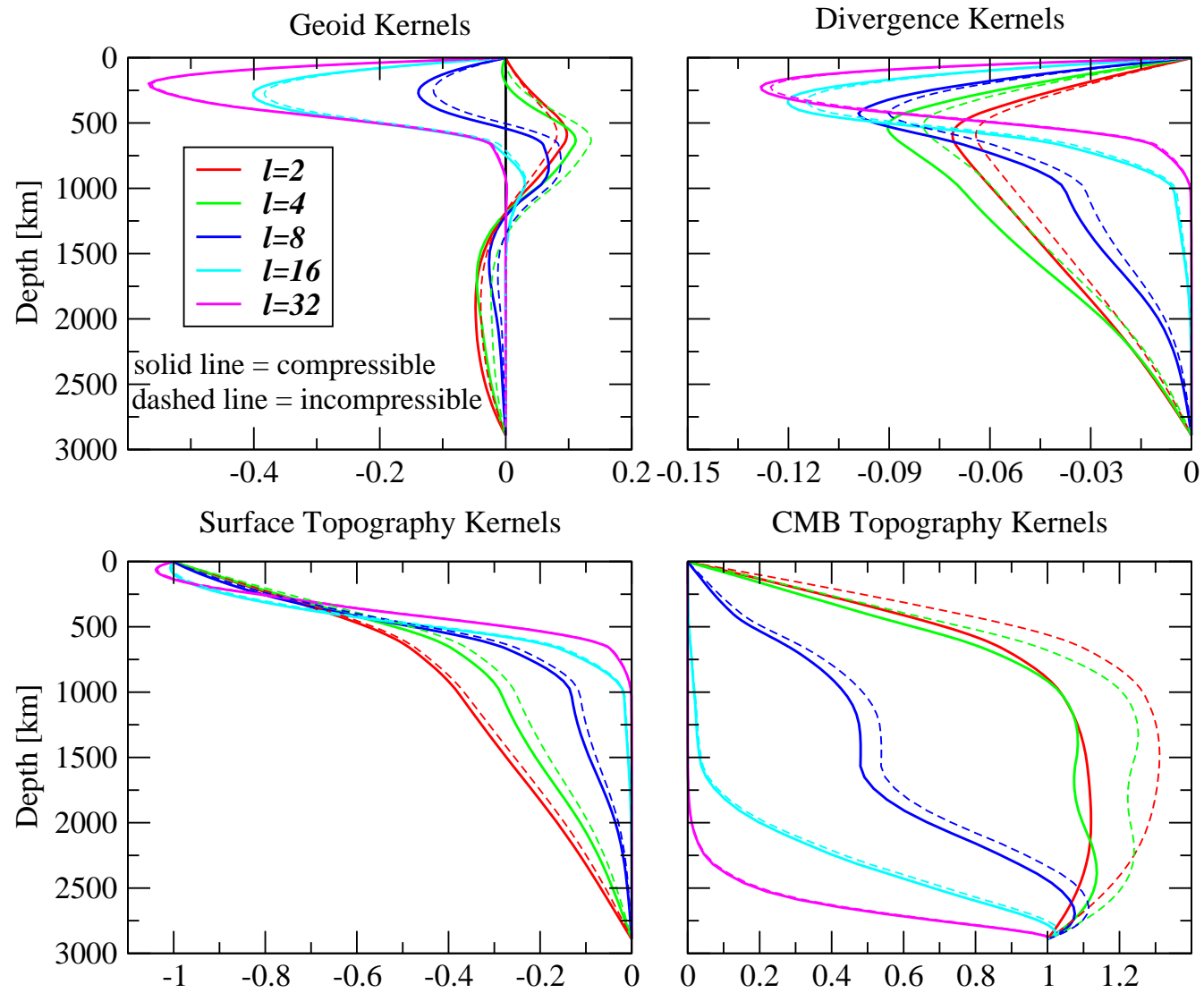


Fig. 13. Geodynamic kernels calculated with the density and viscosity profiles in Fig. 12.

3.2. Predicted geodynamic surface observables based on seismic tomography

We now consider predictions of the convection-related surface observables which may be obtained by convolving the kernels in Fig. 13 with the mantle density anomalies which may be estimated from a global seismic tomography model. For this purpose we will employ the model of S-wave heterogeneity obtained by *Grand* [2002]. We will translate the relative S-velocity perturbations into equivalent density perturbations using a logarithmic scaling factor $d \ln(\rho)/d \ln(V_S)$ derived by *Karato & Karki* [2001] on the basis of mineral physics data and theory. We are therefore assuming that the S-velocity anomalies in the tomography model are primarily *thermal* in origin. The analysis of *Forte & Mitrovica* [2001] suggests that this assumption is a reasonably good approximation, even in the presence of chemical heterogeneity.

The $d \ln(\rho)/d \ln(V_S)$ scaling factor derived by *Karato & Karki* [2001] is shown below in Fig. 14.

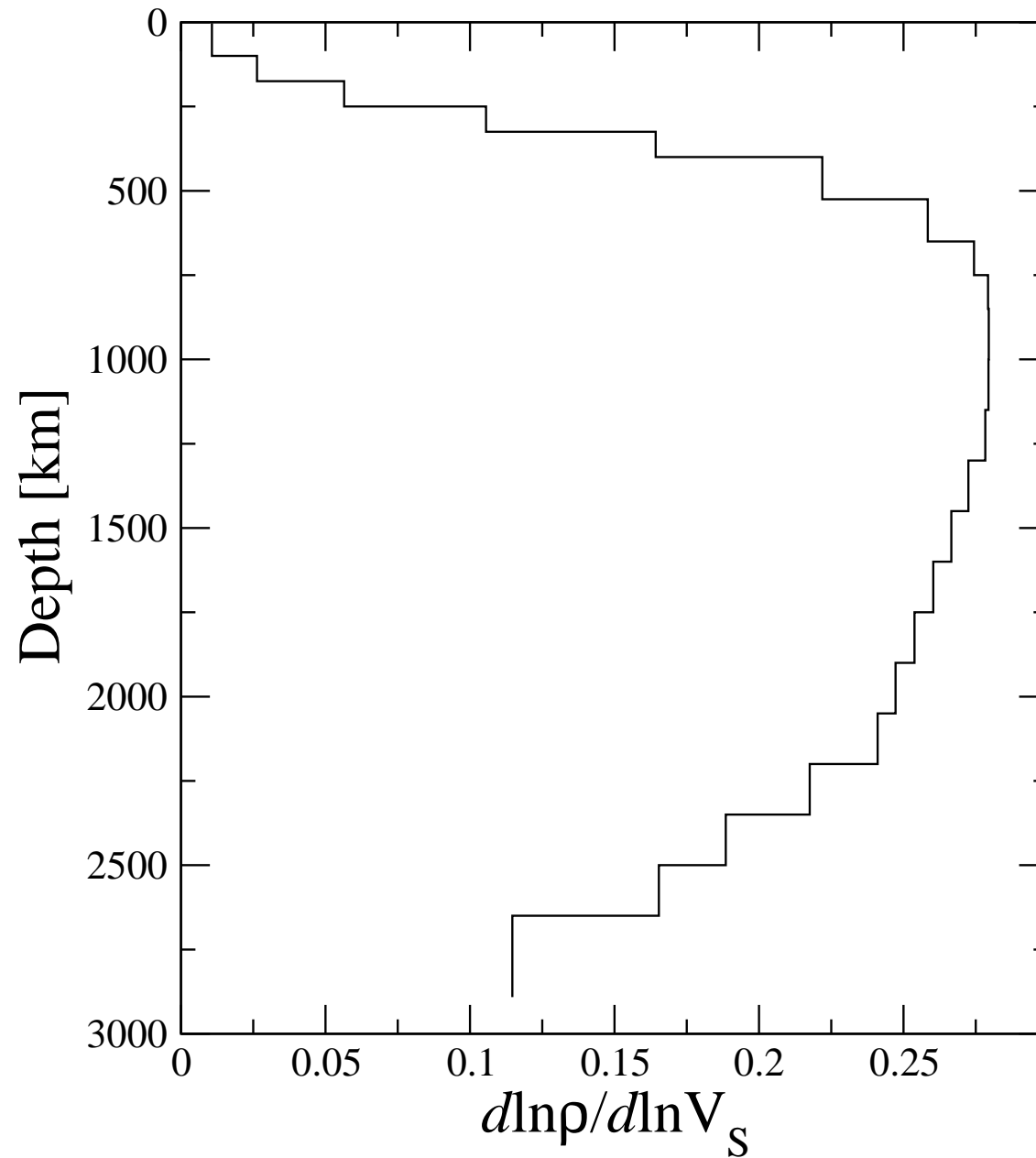


Fig. 14. Mineral physics estimate of thermal density-velocity scaling [Karato & Karki, 2001].

The predicted geoid anomalies we obtain on the basis of these assumptions, are shown below in Fig. 15. We note that the overall amplitude of the predicted anomalies is smaller than the observed anomalies, but the spatial correlation is very good. This amplitude difference has three possible sources: (1) the seismically inferred heterogeneity may be too strongly damped, (2) the estimated value of $d \ln(\rho)/d \ln(V_S)(r)$ (Fig. 14) is too low and/or, 3) the inferred viscosity profile (Fig. 12b) is not appropriate.

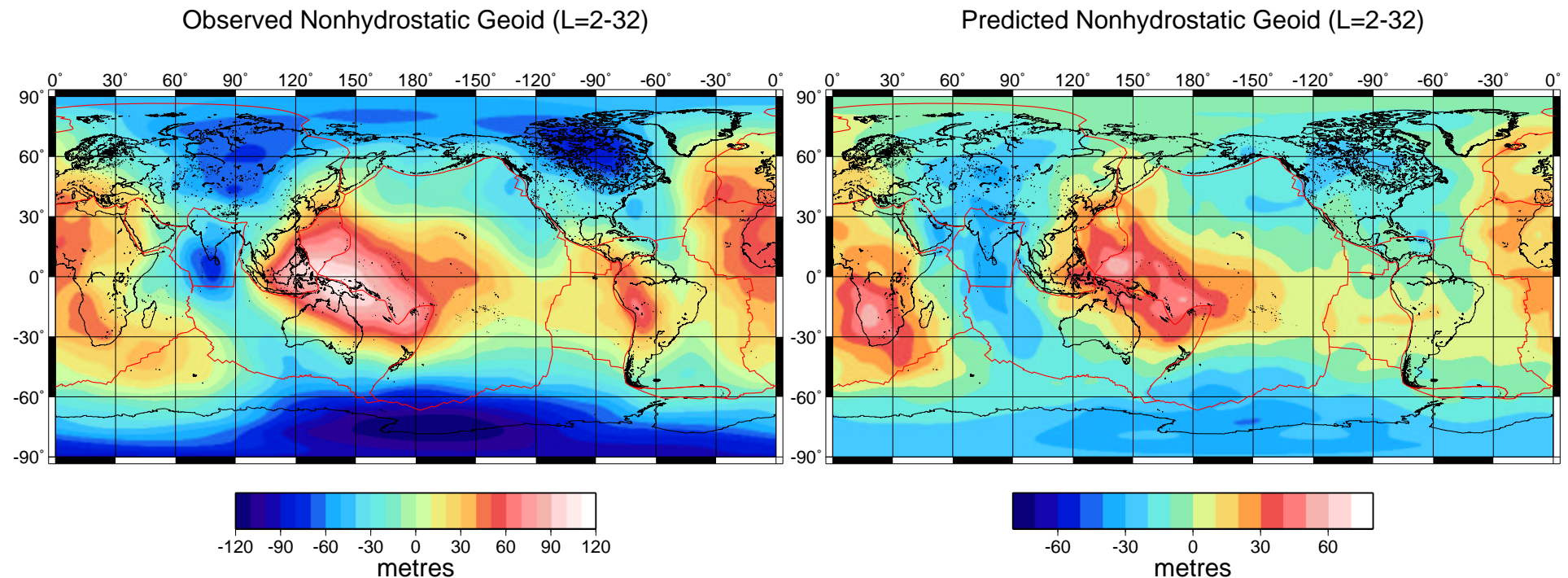


Fig. 15. Observed geoid anomalies and predictions obtained from a tomography-based viscous flow calculation.

All three possible explanations for the amplitude mismatch in Fig. 15 are likely:

- Firstly, the damping of the amplitude of seismic heterogeneity is a natural consequence of tomographic inversion algorithms which require a regularization condition, such as smoothing, to stabilize the inversions [see, for example, *Su et al.*, 1994].
- Second, the viscosity inference in Fig. 12b was obtained on the basis of an earlier, very-long-wavelength global tomography model which differs from the higher-resolution tomography model of *Grand* [2002]. Since the viscosity inverse problem is dependent on the model of mantle heterogeneity, it is possible that the profile in Fig. 12b is not compatible with *Grand's* tomography model.
- The theoretical, mineral-physics estimate of $d \ln(\rho)/d \ln(V_S)$ (Fig. 14) is derived on the basis of a number of assumptions and approximations which may not be fully applicable to the mantle.

We can address the third point, concerning the appropriate $d \ln(\rho)/d \ln(V_S)$ profile, by carrying out a simple inversion of the geodynamic data. The geodynamic data provide *direct, linear constraints* on the density anomalies in the

mantle (see equations 50 – 53), which may be expressed as follows:

$$\delta O_\ell^m = f_\ell \int_b^a K_\ell(\eta(r)/\eta_o; r') (\rho_1)_\ell^m(r') dr' \approx f_\ell \sum_{i=1}^N K_\ell(\eta(r)/\eta_o; r_i) (\rho_1)_\ell^m(r_i) w_i \quad (109)$$

in which δO_ℓ^m is the spherical harmonic coefficient of a geodynamic observable (e.g., geoid anomalies), $K_\ell(\eta(r)/\eta_o; r')$ is the corresponding kernel function, which itself depends on the *relative* (non-dimensional) mantle viscosity profile, and f_ℓ is a factor which depends on the geodynamic observable (see, for example, equation 50). The numerical calculation of integrals is usually carried out with equivalent finite sums, such as in (109) where w_i is a numerical weighting term which depends on the summation algorithm (e.g., Gauss-Legendre quadrature). We may further rewrite expression (109) as

$$\delta O_\ell^m = f_\ell \sum_{i=1}^N w_i K_\ell(\eta(r)/\eta_o; r_i) \left(\frac{\delta V_S}{V_S} \right)_\ell^m(r_i) \frac{d \ln \rho}{d \ln V_S}(r_i) \quad (110)$$

in which $\delta V_S/V_S$ are the shear-velocity anomalies in the mantle and

$d \ln(\rho)/d \ln(V_S)$ is the corresponding velocity-to-density scaling coefficient.

Expression (110) provides the basis for a *discrete, linear* inversion of the geodynamic data δO_ℓ^m to find an optimal velocity-to-density scaling coefficient $d \ln(\rho)/d \ln(V_S)(r_i)$. We may carry out an *Occam* inversion [Constable *et al.*, 1987] of the geodynamic data to find the *smoothest* family of $d \ln(\rho)/d \ln(V_S)$ profiles which are consistent with the data. For this inversion we will employ the tomography model of Grand [2002] (Fig. 4) and we will again employ the MF2 viscosity model (Fig. 12b), while recognizing that it may not be fully compatible with the tomography model. The results of an Occam inversion of the combined nonhydrostatic geoid [Marsh *et al.*, 1990], surface topography [Forte & Perry, 2000], and excess CMB ellipticity [Mathews *et al.*, 2002] data sets, yields the conversion profiles shown below in Fig. 16:

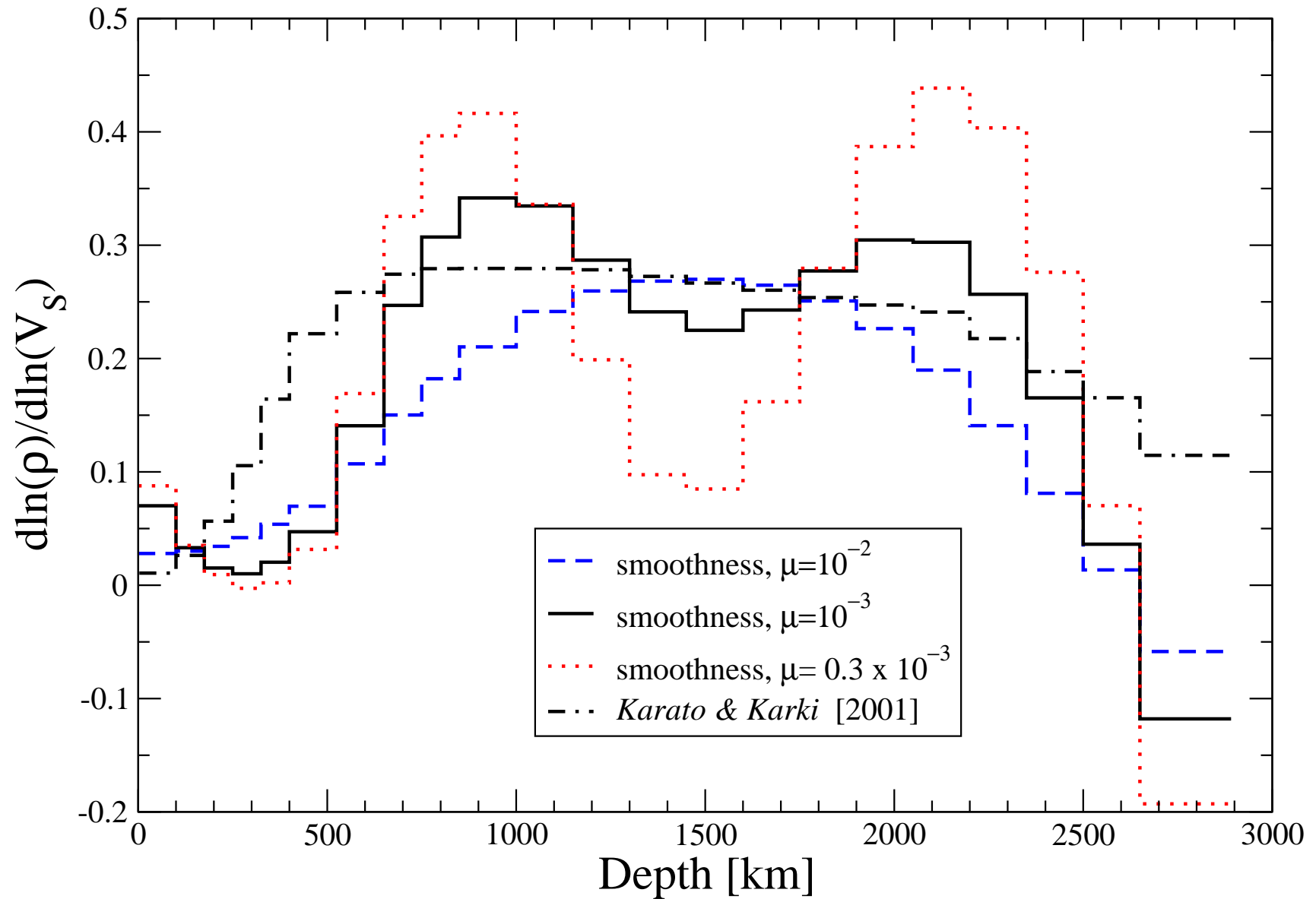


Fig. 16. Velocity-to-density conversions derived from Occam inversion of geodynamic data.

TABLE 1. Fits to geodynamic data, expressed in terms of variance reduction*

$d \ln(\rho)/d \ln(V_S)$ Model [†]	Geoid (Gravity) [‡] [$\ell = 2 - 32$]	Dynamic Topography [§] [$\ell = 1 - 32$]	Excess CMB Ellipticity [#]
<i>Karato & Karki</i>	59% (7%)	7%	1.6 km
$\mu = 10^{-2}$	38% (18%)	34%	0.4 km
$\mu = 10^{-3}$	50% (27%)	30%	0.4 km
$\mu = 0.3 \times 10^{-3}$	58% (31%)	29%	0.4 km

* All predictions employ *Grand's* [2002] tomography model and the *MF2* viscosity inference (Fig. 12b).

† See Fig. 16 for the corresponding $d \ln(\rho)/d \ln(V_S)$ profiles.

‡ The observed geoid and free-air gravity anomalies are both derived from the non-hydrostatic geopotential [*Marsh et al.*, 1990]. The amplitude spectra of the geoid and gravity anomalies are quite different, with the latter having a relatively 'flat' spectrum, which explains why the fits to these two fields differ.

§ The dynamic surface topography is obtained by removing the contribution of the isostatically compensated crustal thickness and crustal density heterogeneity [*Forte & Perry*, 2000].

Based on the free-core nutation analysis of *Mathews et al.* [2002], the Y_2^0 coefficient describing the non-hydrostatic CMB ellipticity is inferred to be -0.4 km (the negative sign indicating an *excess*).

Table 1 shows that the $d \ln(\rho)/d \ln(V_S)$ inference obtained with an Occam smoothing weight of $\mu = 10^{-3}$ provides a good compromise between data fit and model roughness (see Fig. 16). This inference also follows the overall tendency of the *Karato & Karki* [2001] estimate. The dynamic surface topography predicted with this velocity-to-density scaling is shown below:

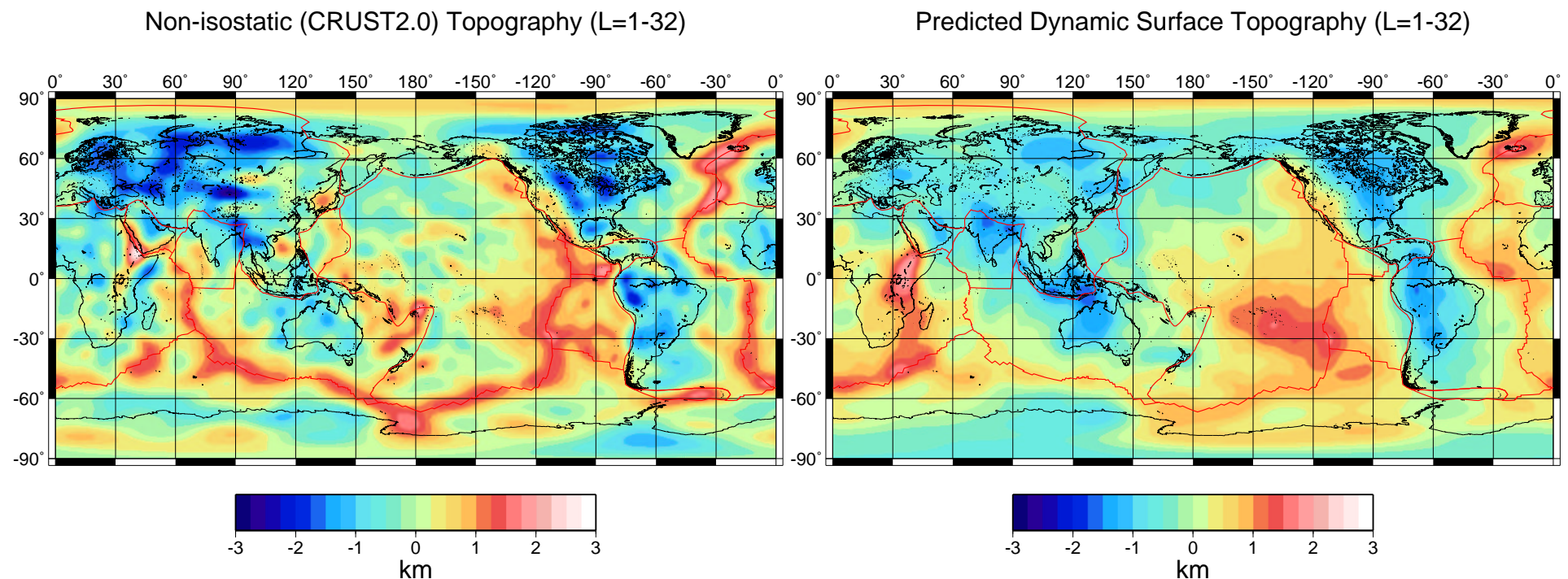


Fig. 17. Isostatically reduced surface topography, based on the CRUST2.0 crustal heterogeneity model, and the predicted dynamic topography obtained from a tomography-based viscous flow calculation.

We next consider the topographic undulations at the CMB which are predicted on the basis of the Occam-inferred velocity-to-density scaling. In the following figure we compare this prediction with the seismically inferred CMB topography obtained by *Boschi & Dziewonski* [2000].

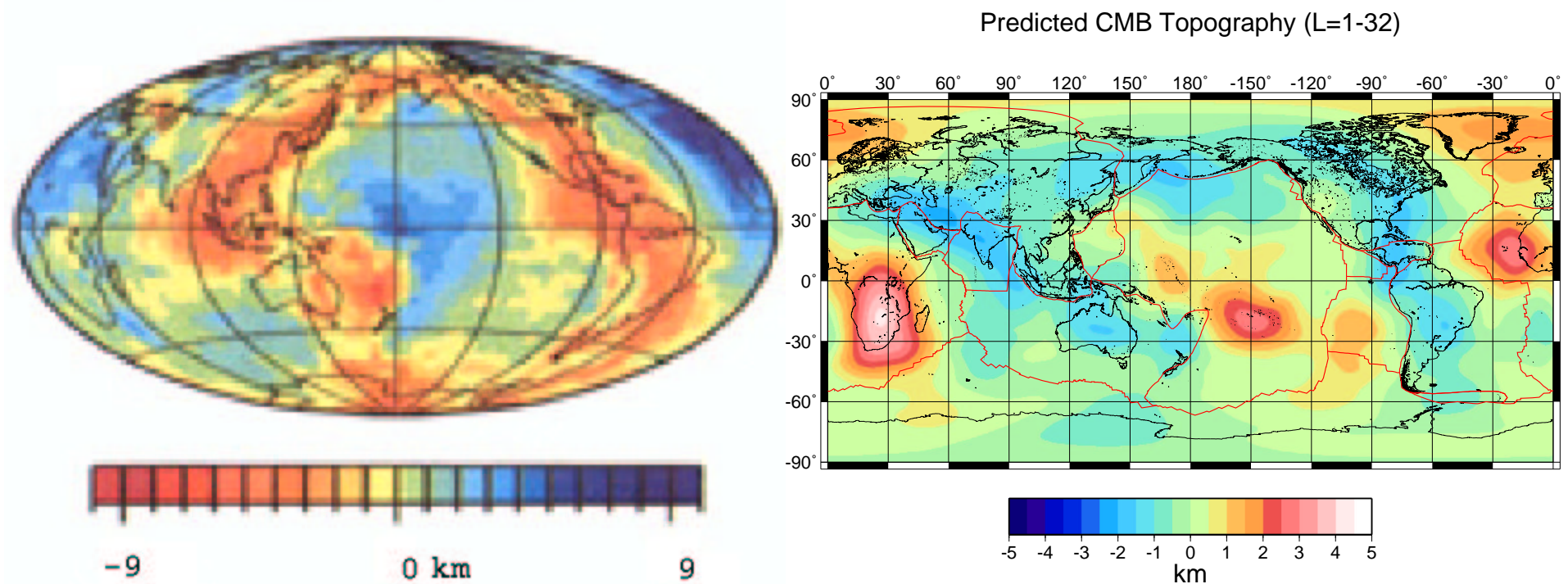


Fig. 18. Seismically inferred CMB topography [*Boschi & Dziewonski, 2000*] and the tomography-based flow prediction.

We will finally consider the horizontal divergence of the predicted surface flow. We will compare this prediction with the observed plate divergence, but we must of course recognize that our flow model does not incorporate the complex surface rheological variations which are required to properly account for the plates and the associated near-surface dynamics.

The treatment of surface plates and lateral viscosity variations be the subject of the next Lecture.

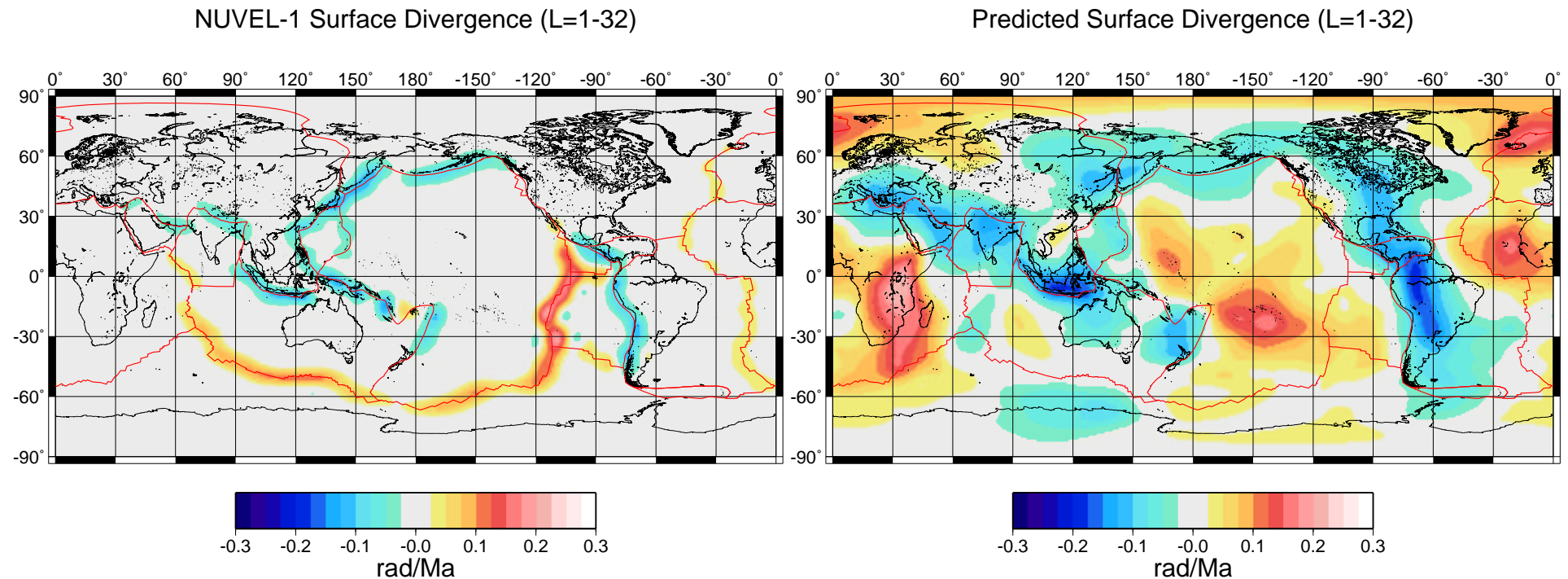


Fig. 19. Horizontal divergence of the NUVEL-1 [DeMets *et al.*, 1990] plate velocities and the tomography-based flow prediction.

4. References

- Akimoto, S., and H. Fujisawa, Olivine–spinel solid solution equilibrium in the system $\text{Mg}_2\text{SiO}_4\text{–Fe}_2\text{SiO}_4$, *J. Geophys. Res.*, **73**, 1467–1479, 1968.
- Backus, G, A class of self-sustaining dissipative spherical dynamos, *Ann. Phys.*, **4**, 372–447, 1958.
- Boschi, L., and A.M. Dziewonski, Whole Earth tomography from delay times of *P*, *PcP*, and *PKP* phases: Lateral heterogeneities in the outer core or radial anisotropy in the mantle? *J. Geophys. Res.*, **105**, 13,675–13,696, 2000.
- Bunge, H.-P., M.A. Richards, C. Lithgow-Bertelloni, J.R. Baumgardner, S.P. Grand, and B.A. Romanowicz, Time scales and heterogeneous structure in geodynamic Earth models, *Science*, **280**, 91–95, 1998.
- Constable, S.C., R.L. Parker, and C.G. Constable, Occam’s inversion: A practical algorithm for generating smooth models from electromagnetic sounding data, *Geophys.*, **52**, 289–300, 1987.
- Corrieu, V., C. Thoraval, and Y. Ricard, Mantle dynamics and geoid Green functions, *Geophys. J. Int.*, **120**, 516–523, 1995.
- Defraigne, P., Internal loading of a compressible Earth: Effect of a solid lithosphere *Phys. Earth Planet. Inter.*, **101**, 303–313, 1997.
- De Mets, C.R., R.G. Gordon, D.F. Argus, and S. Stein, Current plate motions, *Geophys. J. Int.*, **101**, 425–478, 1990.
- Dziewonski, A.M., and D.L. Anderson, Preliminary reference Earth model, *Phys. Earth Planet. Inter.*,

25, 297–356, 1981.

- Forte, A.M., and W.R. Peltier, Plate tectonics and aspherical Earth structure: The importance of poloidal–toroidal coupling, *J. Geophys. Res.*, **92**, 3645–3679, 1987.
- Forte, A.M., and W.R. Peltier, Viscous flow models of global geophysical observables, 1 Forward problems *J. Geophys. Res.*, **96**, 20,131–20,159, 1991.
- Forte, A.M., and J.X. Mitrovica, New inferences of mantle viscosity from joint inversion of long-wavelength mantle convection and post–glacial rebound data, *Geophys. Res. Lett.*, **23**, 1147–1150, 1996.
- Forte, A.M., and H.K.C. Perry, Geodynamic evidence for a chemically depleted continental tectosphere, *Science*, **290**, 1940–1944, 2000.
- Forte, A.M., and J.X. Mitrovica, Deep-mantle high-viscosity flow and thermochemical structure inferred from seismic and geodynamic data, *Nature*, **410**, 1049–1056, 2001.
- Forte, A.M., W.R. Peltier, and A.M. Dziewonski, Inferences of mantle viscosity from tectonic plate velocities, *Geophys. Res. Lett.*, **18**, 1747–1750, 1991.
- Grand, S.P., Mantle shear-wave tomography and the fate of subducted slabs, *Phil. Trans. R. Soc. Lond. A*, **360**, 2475–2491, 2002.
- Hager, B. H., Subducted slabs and the geoid: Constraints on mantle rheology and flow, *J. Geophys. Res.*, **89**, 6003–6015, 1984.
- Hager, B.H., and R.W. Clayton, Constraints on the structure of mantle convection using seismic

observations, flow models, and the geoid, in *Mantle Convection: Plate tectonics and global dynamics*, edited by W. R. Peltier, pp. 657–763, Gordon and Breach (New York), 1989.

- Haskell, N.A., The motion of a viscous fluid under a surface load, *Physics* (N.Y.), **6**, 265–269, 1935.
- Jackson, J.D., *Classical Electrodynamics*, John Wiley (New York), 1975.
- Karato, S., and B.B. Karki, Origin of lateral variation of seismic wave velocities and density in the deep mantle, *J. Geophys. Res.*, **106**, 21,771–21,784, 2001.
- King, S.D., Models of mantle viscosity, in *A Handbook of Physical Constants: Mineral Physics and Crystallography*, edited by T.J. Ahrens, pp. 227–236 AGU Reference Shelf Series, vol. 2, American Geophysical Union (Washington DC), 1995.
- Landau, L.D., and E.M. Lifshitz, *Fluid Mechanics*, vol.6, Pergamon (New York), 1959.
- Liu, L., The post-spinel phase of forsterite, *Nature*, **262**, 770–772, 1976.
- Marsh, J.G., et al., The GEM-T2 gravitational model, *J. Geophys. Res.*, **95**, 22043–22071, 1990.
- Mathews, P.M., T.A. Herring, and B.A. Buffett, Modeling of nutation and precession: New nutation series for nonrigid Earth and insights into the Earth's interior, *J. Geophys. Res.*, **107**(B4), 2068, doi:10.1029/2001JB000390, 2002.
- McKenzie, D.P., J.M. Roberts, and N.O. Weiss, Convection in the Earth's mantle: Towards a numerical simulation, *J. Fluid Mech.*, **62**, 465–538, 1974.
- Mitrovica, J.X., Haskell[1935] revisited, *J. Geophys. Res.*, **101**, 555-569, 1996.

- Mitrovica, J.X., and A.M. Forte, Radial profile of mantle viscosity: Results from the joint inversion of convection and postglacial rebound observables, *J. Geophys. Res.*, **102**, 2751–2769, 1997.
- Panasyuk, S.V., B.H. Hager, and A.M. Forte, Understanding the effects of mantle compressibility on geoid kernels, *Geophys. J. Int.*, **124**, 121–133, 1996.
- Parsons, B., and S. Daly, The relationship between surface topography, gravity anomalies, and the temperature structure of convection, *J. Geophys. Res.*, **88**, 1129–1144, 1983.
- Pekeris, C.L., Thermal convection in the interior of the Earth, *Mon. Not. R. Astron. Soc., Geophys. Suppl.* **3**, 343–367, 1935.
- Phinney, R.A., and R. Burridge, Representation of the elastic-gravitational excitation of a spherical Earth model by generalized spherical harmonics, *Geophys. J. R. Astron. Soc.*, **34**, 451–487, 1973.
- Ranalli, G., and B. Fischer, Diffusion creep, dislocation creep, and mantle rheology, *Earth Planet. Sci. Lett.*, **34**, 77–84, 1984.
- Ricard, Y., L. Fleitout, and C. Froidevaux, Geoid heights and lithospheric stresses for a dynamic Earth, *Ann. Geophys.*, **2**, 267–286, 1984.
- Richards, M.A., and B.H. Hager, Geoid anomalies in a dynamic Earth, *J. Geophys. Res.*, **89**, 5987–6002, 1984.
- Ringwood, A.E. Phase transformations and mantle dynamics, *Earth Planet. Sci. Lett.*, **14**, 233–241, 1972.
- Ringwood, A.E., and A. Major, Synthesis of Mg_2SiO_4 – Fe_2SiO_4 spinel solid solutions, *Earth Planet. Sci. Lett.*, **1**, 241–245, 1966.

- Sammis, C.G., J.C. Smith, G. Schubert, and D.A. Yuen, Viscosity-depth profile of the Earth's mantle: Effects of polymorphic phase transitions, *J. Geophys. Res.*, **82**, 3747–3761, 1977.
- Su, W.-J., R.L. Woodward, and A.M. Dziewonski, Degree 12 model of shear velocity heterogeneity in the mantle, *J. Geophys. Res.*, **99**, 6945–6980, 1994.